LBL-7622

VALENCE BAND PHOTOEMISSION STUDIES OF CLEAN METALS

Paul Sherman Wehner
(Ph. D. thesis)

April 1978

Prepared for the U. S. Department of Energy
under Contract W-7405-ENG-48

LBL-7622

VALENCE BAND PHOTOEMISSION STUDIES OF CLEAN METALS

Contents

ABSTRACT v

I. INTRODUCTION 1

References 5

Figures 7

II. EXPERIMENTAL APPARATUS AND TECHNIQUES 8

A. Spectrometers 8

B. The Photon Source 12

C. Sample Preparation Techniques 14

References 16

Tables 18

Figures 22

III. ANGLE-RESOLVED PHOTOEMISSION FROM Cu SINGLE CRYSTALS IN THE PHOTON ENERGY RANGE 32 TO 200 eV 34

A. Introduction 34

B. Normal Emission 35

B.1 Experimental 35

B.2 Experimental Results 36

B.3 Discussion 38

C. Non-Normal Emission 46

References 51

Table I 54

Figures 58

IV. BREAKDOWN OF THE DIRECT TRANSITION MODEL 71
A. Introduction 71
B. Momentum Broadening 72
C. Thermal Disorder 74
D. Band Mixing 77
References 81
Figures 85
V. ANGLE-RESOLVED X-RAY PHOTOEMISSION FROM SINGLE CRYSTALS . 95
A. Introduction 95
B. Experimental Details and Results 95
C. Matrix Element Model 96
D. Discussion of Results 102
Appendix A 104
References 106
Table I 109
Figures 111
Acknowledgments 113

VALENCE BAND PHOTOEMISSION STUDIES OF CLEAN METALS

Paul Sherman Wehner

Materials and Molecular Research Division
Lawrence Berkeley Laboratory
and
Department of Chemistry
University of California
Berkeley, California 94720

ABSTRACT

The application of Angle-Resolved Photoelectron Spectroscopy (ARPES) to crystalline solids and the utilization of such studies to illuminate several questions concerning the detailed electronic structure of such materials, are discussed. Specifically, by construction of a Direct Transition (DT) model and the utilization of energy-dependent angle-resolved normal photoemission in the photon energy range 32 eV $\leq h\nu \leq$ 200 eV, the bulk band structure of copper is experimentally mapped out along three different directions in the Brillouin Zone; Γ to K, Γ to L, and Γ to X. In addition, various effects which influence the obtainable resolution in $\vec{k}$-space, namely, thermal disorder, momentum broadening, and band mixing, are discussed and are shown to place severe limitations on the applicability of the DT model. Finally, a model for Angle-Resolved X-ray Photoelectron Spectroscopy (ARXPS) based on the symmetry of the initial-state wavefunctions is presented and compared to experimental results, obtained from copper single crystals.

I. INTRODUCTION

Knowledge of the electronic structure of materials is of fundamental importance if a detailed understanding of their chemical and physical properties is to be obtained. This dissertation will be concerned with a technique, Photoelectron Spectroscopy (PES), which during the past few years has proven to be of considerable value in the determination of such information. In particular, this thesis will deal with the application of Angle-Resolved Photoelectron Spectroscopy (ARPES) to crystalline metals, and discuss exactly how the results of such studies can be used to illuminate several important questions concerning the detailed electronic structure of such materials.

The important experimental features of ARPES, as applied to crystalline solids, are summarized in Fig. 1. The angle-resolved photoemission (ARP) experiment essentially consists of irradiating the sample under investigation with nearly monoenergetic photons of energy $h\nu$, causing electrons which have binding energies less than $h\nu$ to be ejected. Outside the solid, the electrons are then characterized in terms of their kinetic energy and the propagation angles θ and ϕ. In this way information on both the electron's energy, and its $\vec{k}$-vector (the latter being related to the propagation direction) is obtained.

The apparatuses used to perform these experiments will be described in Chapter II. Briefly, four areas of experimental detail may be noted. First, the detection of the photoemitted electron requires high vacuum, and sample cleanliness further necessitates ultra-high vacuum conditions; the latter are achieved by use of a stainless steel bakeable bell jar

and suitable vacuum pumps. The excitation source, our second subsystem, may be either a discrete line source (e.g., a characteristic x-ray) or a continuous photon energy source (i.e., synchrotron radiation). A device for energy analysis of the photoelectrons and the associated electronics to collect and store the data form the third component of the spectrometer. As both the mass and charge of the electron are known, we may determine its energy either by momentum analysis, i.e., using time-of-flight or magnetic mass spectrometric techniques, or more directly by electrostatic energy analysis. Finally, the sample for the experiments must be microscopically clean and single crystalline in form. These requirements are achieved by a combination of pre-analysis preparation and *in situ* cleaning.

In Chapter III experimental results obtained for photoemission from the valence bands of the three low-Miller-index crystal faces of copper as a function of the incident photon energy ($32\ eV \leq h\nu \leq 200\ eV$) will be presented. In addition, it will be demonstrated how the kinetic energy and wavevector of the electron outside the crystal can be related to its initial state energy and wavevector inside the crystal. The theoretical framework for these studies is based on Koopman's Theorem (1) and a one-electron picture of PES. Essentially, the semi-classical three-step model of PES is employed (2). The first step involves excitation of an electron from its initial state to a conduction band in the solid; one generally assumes here both dipole transitions and an absence of readjustment in the electron density. The second and third steps are, respectively, transport of the excited electron to the surface, and escape into vacuum. These last steps are

usually either neglected entirely or treated in some *ad hoc* phenomenological way. Within such a framework, it will be shown how the experimental results may be understood by the construction of a "Direct Transition" (DT) model.

The fourth Chapter of this thesis will deal with three effects which influence the resolution in $\vec{k}$-space and therefore have a severe impact on the simple model developed in Chapter III. The first effect we shall discuss is that resulting from the finite mean-free-path of an electron in a solid. Shortening of the mean-free-path results in an uncertainty or "smearing" in the value of the component of $\vec{k}$ perpendicular to the surface of the sample (3); while this does not lead to a complete breakdown of the DT model, it nevertheless implies a lessening of the $\vec{k}$-resolution obtainable. Secondly, the effect of thermal disorder (4) on the ARP spectrum will be discussed, and be shown to result in a complete breakdown of the DT model at temperatures large compared to the Debye temperature of the solid. Finally, for photoemission at high photon energies, i.e., Al Kα (1486.6 eV), mixing of the bands in the final state will be shown to be important and again lead to a breakdown of the DT model.

In the final Chapter of this thesis, a model for Angle-Resolved X-Ray Photoelectron Spectroscopy (ARXPS) based on the symmetry properties of the initial state wavefunctions will be presented. In particular, with the assumption of a plane wave final state and a tight-binding initial state, an analytical expression will be derived which demonstrates that, in general, an angle-resolved x-ray photoemission spectrum

obtained from a d-band metal which crystallizes in a face-centered-cubic structure represents a linear combination of the t_{2g} and e_g projections of the initial density of states.

REFERENCES

1. T. Koopmans, Phsica 1, 104 (1933).

2. C. N. Berglund and W. E. Spicer, Phys. Rev. 136, A1030 (1964) and ibid. 136, A1044 (1964); A. J. Blodgett and W. E. Spicer, Phys. Rev. 158, 514 (1967); W. F. Krolikowski and W. E. Spicer, Phys. Rev. 185, 882 (1969).

3. P. J. Fiebelman and D. E. Eastman, Phys. Rev. B10, 4932 (1974); B. Feuerbacher and R. F. Willis, J. Phys. C9, 169 (1976).

4. N. J. Shevchik, private communication.

FIGURE CAPTION

Fig. 1 Schematic illustration of the important features of an angle-resolved photoemission experiment for a solid. Photons of energy $h\nu$ impinge on a sample, causing electrons to be ejected which are then characterized in terms of their kinetic energy and the propagation angles θ and ϕ.

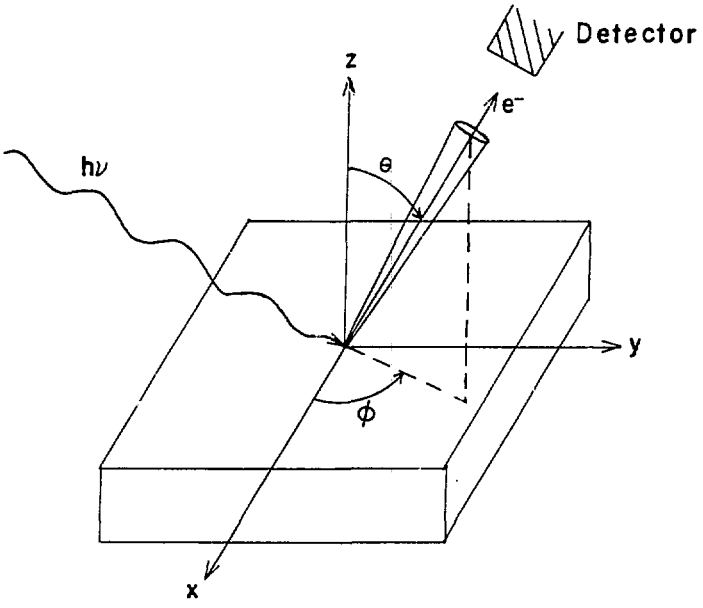

XBL 784-7990

Figure 1

II. EXPERIMENTAL APPARATUS AND TECHNIQUES

A. Spectrometers

There are several excellent reviews in the literature concerning the design principles of photoelectron spectrometers (1-4); therefore, only those aspects as are immediately pertinent to our discussion will be mentioned. The photoemission experiments reported in this thesis have been performed on two different instruments. An HP 5950A ESCA spectrometer, modified for ultra-high vacuum capabilities, was employed for the experiments reported in Chapter V and the latter part of Chapter IV. This spectrometer has been described in full detail previously (5) and the reader is referred to that work for a complete description of the machine. Briefly, the instrument makes use of Aℓ Kα x-rays ($h\nu$ = 1486.6 eV) and a dispersion compensation scheme to achieve monochromatization. It is pumped by a combination of three noble ion pumps (30 ℓ/sec, 110 ℓ/sec, and 220 ℓ/sec) and a 350 ℓ/sec titanium sublimation pump, and is capable of achieving and maintaining a base pressure of 5×10^{-11} torr. A hemispherical electrostatic analyzer (15.5 cm central radius) is used for energy analysis of the photoejected electrons, and the data are collected and stored in a multichannel analyzer.

For the experiments conducted at the Stanford Synchrotron Radiation Laboratory (SSRL), reported in Chapters III and IV, a second, portable photoelectron spectrometer was constructed and used. This spectrometer is shown in Figs. 1 and 2, and consists essentially of three major components; an ultra-high vacuum (UHV) chamber, an electron energy analyzer capable of both angle-integrated and angle-resolved modes of operation, and a data acquisition and storage system. The UHV chamber is a

stainless steel bell jar with a variety of ports on it to allow for the installation of the electron energy analyzer, the sample manipulator, the ion pump, and other fixtures. It is pumped by a combination of a 700 ℓ/sec titanium sublimation pump (TSP) and a 220 ℓ/sec noble ion pump, and is capable of obtaining a base pressure of $\sim 3.0 \times 10^{-11}$ torr. To reach this pressure it is necessary to "bake" the system, which is accomplished by wrapping the chamber and pumps with electrical heating tapes and aluminum foil. Typically, the system is baked at 200° C into an external 500 ℓ/sec noble ion pump for ~24 hours, while its pumps are off. After this stage, the ion pump and TSP are flashed on and off several times and all the filaments in the system are turned on to expel residual adsorbed gases. The system is then sealed off onto its own pumps and allowed to bake for another day. Finally, the system is allowed to cool (pumps first), with the TSP operating at a duty cycle of ~15%.

The electron energy analyzer, the second major component of our system, is a double-pass cylindrical mirror analyzer (CMA) with a hemispherical retarding grid (Physical Electronics Model PHI 15-255G). This analyzer is operated in the retarding (constant resolution) mode for photoelectron measurements; this type of scheme is shown in Fig. 3. In the retarding mode the energy of the photoejected electrons is first reduced with the retarding field analyzer and then measured accurately with the double-pass CMA. In this way, the energy resolution (ΔE) is significantly enhanced and constant throughout the spectrum; the energy resolution in this mode of operation is determined by the pass energy (E_p) employed and is given by the relation $\Delta E = .016 \times E_p$. Because the

signal levels are usually very low when performing high resolution energy analysis, the preferred detection system is one in which pulse counting is employed rather than detecting the analog signal. This is discussed in greater detail later.

The analyzer also possesses a co-axial, internal electron gun which can be used both as an excitation source for Auger electron analysis and to align the sample (the sample position is very critical for obtaining the maximum count rate and resolution). For Auger analysis the PHI analyzer is normally operated in the non-retarding mode, i.e., the hemispherical grid is held at ground potential, and a smaller aperture is placed between the two CMA's, resulting in an energy resolution which is dependent on the kinetic energy (E_K) of the detected electrons; this is given by the relation $\Delta E = .006 \times E_K$. Since the Auger spectrum is much more pronounced if the derivative of the energy distribution is recorded rather than the energy distribution itself, a small a.c. component (frequency of ~10 kHz and amplitude of 0-10 volts peak-to-peak) is added to the voltage of the outer cylinder, and a lock-in amplifier is used in the detection circuit. This is illustrated in Fig. 4 where a block diagram for this mode of operation is shown.

The PHI analyzer was adapted for angle-resolved measurements by placing a stainless-steel shield with an eleven degree slit aperture on the front of the analyzer; the geometrical arrangement of the slit is shown in Fig. 5. The modified analyzer has an angular acceptance of approximately ±5°; the angular acceptance in the horizontal plane, ±6°, is defined by the inherent acceptance of the PHI (6), while that in the vertical plane, ±4°, is defined by slit aperture. It was found that the

shield decreases the collecting efficiency of the PHI by approximately a factor of 360/11, as expected on purely geometrical grounds. As an added bonus, however, it was found that the aperture improves the energy resolution of the PHI analyzer by a factor of ∿2. This is illustrated in Fig. 6 where spectra taken with and without the shield of the spin-orbit split 4d-doublet in indium are shown for different electron pass energies.

A diagram of the spectrometer detection and data-handling systems for operation in the pulse counting mode is shown in Fig. 7. The electron current passing through the final aperture of the CMA is first amplified by an electron multiplier (Galileo spiraltron electron multiplier Model #4719); the resulting cascade (gain $\sim 10^7$) impinges on a Faraday cup, causing a momentary charge build-up. The resulting voltage spike (typically 30-40 ns in duration and 16 mV in amplitude) then passes through an a.c. decoupling box into a preamp/discriminator; the latter is composed of three main components and is shown in Fig. 8 in block form. (The 120-ohm cable used to interconnect the Faraday cup and the decoupling box should be kept as short as possible. The performance of the preamp depends critically on the capacitance of the system.) The voltage pulse first enters a fast video amplifier which performs two functions; 1) it amplifies the signal by a factor of ten and, 2) it is a narrow band filter in the megahertz range (1-100 MHz) and therefore eliminates all 60-cycle noise. Then, if the signal exceeds a certain discriminator level (which is adjusted to be above dark noise), it is "shaped" into a standard counting pulse (width and amplitude) by a voltage comparator, and is further amplified by a line

driver. The resulting five volt pulse can then be fed into a frequency counter or directly into the memory of an MCA. (For work requiring an analog signal, e.g., Auger analysis, the preamp/discriminator is replaced by an operational amplifier [see Fig. 4] which acts as a current to voltage transducer.)

The main component of the data-handling system is a digital addresser which was designed and built at LBL by Mr. Joseph Katz. The unit provides: 1) a digital voltage ramp with eight different step sizes (17.4 mV/step to 2.22 V/step, in multiples of 2); 2) five different data collection times (.24, .47, .94, 1.9, and 3.9 sec/point), and; 3) the necessary control signals so that electron counts can be accumulated in 256, 512, 1024, 2048, or 4096 channels of an MCA, or, as in the case of Auger analysis, displayed directly on an X - Y recorder. The option of scanning the same energy region repetitively is also provided; we have taken spectra continuously for as long as eight hours, which corresponds to several hundred scans. Finally, the data stored in the MCA can be transferred to an X - Y point plot, a magnetic tape, or paper tape.

B. The Photon Source

A number of electron storage rings that can provide synchrotron radiation for photoemission studies are now available or under construction throughout the world (7). Among these, a smaller group of intermediate- and high-energy machines affords the possibility of bridging the entire gap between ultraviolet and x-ray energies available from laboratory sources. SSRL (8) has the capability of doing ultra-high vacuum photoemission studies up to and somewhat beyond the carbon K-edge

of 280 eV. No facility has the capability at present to do photoemission at higher energies; i.e., all the way up to x-ray energies. The work reported in Chapters III and IV was carried out in the 32-250 eV range using the 4° port of Beam Line I at SSRL.

The grazing incidence monochromator ("grasshopper") installed on the 4° port (9) is equipped with a 600 ℓ/mm grating, yielding high intensity radiation with sufficient resolution (<1 eV) for photoemission studies between 32 and about 280 eV. Above 280 eV the intensity decreases dramatically due to carbon contamination on the reflecting surfaces. Fig. 9 shows the transmission of the grasshopper monochromator measured as the photocurrent of an Al_2O_3 photodiode (10) as a function of photon energy. To obtain the absolute flux out of the monochromator, the curve shown in Fig. 9 must be corrected by the photoyield of Al_2O_3 which, unfortunately, is known only for $h\nu \leq 160$ eV (11). Fig. 10 shows the quantum efficiency of our detector in the range $10 \text{ eV} \leq h\nu \leq 160$ eV (11). Since the quantum efficiency varies by less than ±20% between 40 and 160 eV, Fig. 9 should describe the energy variation of the photon flux fairly accurately. Table I lists the photon flux (photons sec^{-1} $mA^{-1}mrad^{-1}$) emerging from the monochromator in the energy range 32-290 eV (7), calculated from the cathode current of the photodiode utilizing the Al_2O_3 quantum efficiency values (also in Table I).

In order to compare the photon flux emitted by the storage ring SPEAR to that emerging from the monochromator, the resolution of the monochromator must be considered. The monochromator bandwidth ΔE (in eV) is theoretically given by the relation (13)

$$\Delta E = S \cdot 10^{-6} E^2 , \qquad (1)$$

where E is the photon energy in eV. Values for ΔE in the range 32-290 eV are listed in Table I. Integrating the respective $\Delta E/E$ values to yield a 10% bandwidth ($\Delta E/E = 0.1$) we obtain the photon flux values listed in the last column of Table I. These values can now be directly compared to the flux emitted by SPEAR which is shown in Fig. 11 as a function of beam energy. During the course of our experiments SPEAR operated at 3.3 GeV producing a photon flux of 2-5 x 10^{12} photons sec^{-1} $mrad^{-1}mA^{-1}$ (10% bandwidth)$^{-1}$ (see Fig. 11) in the energy range 30-300 eV. Thus, for maximum monochromator transmission ($h\nu$ = 150 eV) the efficiency of the optical system (consisting of 4 mirror reflections and the diffraction grating) is about 0.15%. This is actually an upper limit since contributions from higher order harmonics and scattered light to the transmitted radiation have been ignored. Also we have assumed that the bandwidth of the monochromator is given by Eq. (1), which is the optimum value obtainable.

C. Sample Preparation Techniques

The need to prepare atomically clean, well characterized specimens makes sample preparation one of the most important experimental aspects of PES studies of solids; atomically clean surfaces are necessitated by the sampling depth in PES which, as can be seen from Fig. 12 (14), is on the order of a few lattice spacings. Methods for preparing such samples have been discussed in full detail by S. P. Kowalczyk (5), and the reader is referred to that work for a complete discussion; we shall restrict our attention only to those techniques pertinent to the work reported here.

The samples employed in these investigations reported here were in the form of single crystals, and were spark-cut from single-crystalline rods which had been zone-refined to yield low levels of impurities. The orientation of the crystals was determined by the Laue back-reflection x-ray technique, and was within ±1.0° of the reported orientation. Prior to insertion into the UHV spectrometer, the samples were mechanically polished to 1 μm smoothness and etched, see Table II for the various etching agents and periods necessary to remove the damage layer formed by the polishing. A mild Ar^+ bombardment *in situ*, followed by annealing at *ca.* 600°C, was found to be sufficient to clean both Cu and Au crystals. Platinum crystals, however, were found to be more difficult to clean, and required oxidation treatments ($\sim 5 \times 10^{-6}$ torr of oxygen and sample temperatures of *ca.* 800° C) to remove residual carbon contamination. The resulting oxide layer formed by this treatment could easily be removed by raising the temperature of the sample very briefly (less than 1 minute) to 1000° C. Finally, the techniques of Auger electron spectroscopy and x-ray photoelectron spectroscopy were used to monitor sample cleanliness.

REFERENCES

1. B. Wannberg, U. Gelius, and K. Siegbahn, J. Phys. E 7, 149 (1974).
2. K. D. Sevier, Low Energy Electron Spectroscopy (Wiley-Intersciences, New York, 1972).
3. M. S. Mladjenovie, Adv. Elect. Phys. 30, 43 (1971).
4. E. M. Purcell, Phys. Rev. 54, 818 (1938).
5. S. P. Kowalczyk, Ph.D. Thesis, LBL-4319 (1976).
6. P. W. Palmberg, J. Electron Spectrosc. 5, 691 (1974).
   The value $\Delta\alpha = 6°$ for the acceptance of the PHI analyzer quoted in this reference is incorrect and should read $\Delta\alpha = 12°$ or $\alpha = (42.3 \pm 6)°$. It should also be noted that the PHI used in our studies (Model PHI 15-2556) does not accept electrons equally into its 360° acceptance cone. There are posts in four (1.5, 4.5, 7.5, and 10.5 o'clock) positions inside the analyzer which block electrons along the respective trajectories. This fact has to be considered when rotating the slit for angle resolved studies. For the measurements reported here the slit-aperture was fixed in the 3 o'clock position and therefore the posts had no effect on the measurements.
7. M. L. Perlman, E. M. Rowe, R. E. Watson, Physics Today, July 1974, p. 30.
8. H. Winick in Vacuum Ultraviolet Radiation Physics, (ed. E. E. Koch, R. Haensel, and C. Kunz) Pergamon Vieweg 1974, p. 776.
9. F. C. Brown, R. Z. Bachrach, S. B. M. Hagström, N. Lien, and C. H. Pruett, in Ref. 8, p. 785.

10. E. B. Saloman, D. L. Ederer, Applied Optics 14, 1029 (1975).

11. National Bureau of Standards (NBS) Report of Calibration for our diode in the range 10 eV ≤ hν ≤ 66 eV (unpublished). Above 66 eV the values of W. Gudat, G. Kunz, and W. Lenth, in Ref. 8, p. 725, which were normalized to the NBS calibration values at 50 and 60 eV were used.

12. During the course of the measurements of the photon flux SPEAR operated at 3.3 GeV and ∿30 ma. In addition, the grasshopper monochromator utilizes about 2 mrad of radiation; therefore, the actual flux (photons/sec) was about a factor of 60 higher than the values listed in column 3 of Table I.

13. Here a constant bandpass of 0.1Å has been assumed (see Ref. 9). The relation $\Delta\lambda/\lambda = \Delta E/E$ then yields Eq. (1) directly.

14. I. Lindau and W. E. Spicer, J. Electron Spectrosc. 3, 409 (1974); C. R. Bundle, Surf. Sci. 48, 99 (1975); I. Lindau, P. Pianetta, K. Y. Lu, and W. E. Spicer, J. Electron Spectrosc. 8, 487 (1976).

Table I. Photon Flux and Energy Resolution for SSRP 4° Line Monochromator

Photon energy (eV)	Quantum efficiency of detector	$\frac{\text{photons}}{\text{sec}\cdot\text{mA}\cdot\text{mrad}}$ [c] (10^7)	Monochromator [d] bandwidth ΔE (eV)	$\frac{\text{photons}}{\text{sec}\cdot\text{mA}\cdot\text{mrad}\cdot 10\%\ \text{bandwidth}}$ [c] (10^9)
32	0.112[a]	0.5	0.008	2.0
50	0.079[a]	1.6	0.02	3.9
70	0.062[a]	2.7	0.04	4.8
90	0.060[a]	4.0	0.07	5.6
110	0.070[a]	5.7	0.10	6.5
130	0.067[a]	7.6	0.14	7.3
150	0.060[a]	9.0	0.18	7.5
170	0.05[b]	8.6	0.23	6.3
190	0.05[b]	6.4	0.29	4.2
210	0.05[b]	5.7	0.35	3.4
230	0.05[b]	4.9	0.42	2.6
250	0.05[b]	4.4	0.50	2.2
270	0.05[b]	3.5	0.60	1.6
290	0.05[b]	0.8	0.70	0.3

a) See reference 11.
b) In lack of measured values for the quantum efficiency above 155 eV a constant value of 0.05 has been assumed.
c) See reference 12.
d) Calculated according to Equation (1).

Table II. Etching Agents

Elements	Etching Agent	Period of Etch
Cu	HNO_3 [a]	∿ 30 sec.
Au	Cold aqua regia	∿ 30 min.
Pt	Hot aqua regia	∿ 30 min.

a) A solution composed of equal parts by volume of NH_4OH; H_2O; H_2O_2(3%) has recently been found to yield smoother surfaces for copper than HNO_3.

FIGURE CAPTIONS

Fig. 1 Overall view of the portable photoemission chamber.

1) Cryopumps;

2) External 500 ℓ/sec noble ion pump;

3) Cylindrical mirror analyzer (Physical Electronics Model PHI 15-255G);

4) Sample manipulator (Physical Electronics Model PHI 10-503);

5) 220 ℓ/sec noble ion pump;

6) 700 ℓ/sec titanium sublimation pump.

Fig. 2 Close-up view of a sample in position for photoemission measurements.

Fig. 3 Block diagram for operation of the CMA in retarding (constant resolution) mode.

Fig. 4 Block diagram for operation of the CMA in derivative (Auger) mode.

Fig. 5 The geometrical arrangement of the slit aperture (shield) on the CMA. The modified analyzer has an angular resolution of *ca.* ±5°. The shield is held in position on the inner mu-metal shield by two clamps.

Fig. 6 a) Experimental spectra obtained as a function of the analyzer pass energy (E_p) of the spin-orbit split 4d-doublet in indium, without the slit aperture on the CMA.

b) Experimental spectra obtained as a function of the analyzer pass energy of the In 4d-doublet, with the slit aperture in position. The energy of the incident radiation was 70 eV.

Fig. 7 Block diagram of the portable spectrometer's detection and data handling systems for operation in the pulse-counting mode.

Fig. 8 Block diagram of the preamp/discriminator circuit.

Fig. 9 Transmission function of the monochromator located on the 4° port on Beam Line 1 at SSRL measured as the photocurrent from an NBS-$A\ell_2O_3$ photodiode. To obtain the absolute flux out of the monochromator, the curve must be corrected by the quantum efficiency of $A\ell_2O_3$ in this photon energy range.

Fig. 10 Quantum efficiency of $A\ell_2O_3$ in the photon energy range 10-160 eV (cf. Ref. 11).

Fig. 11 Spectral distribution of synchrotron radiation emitted from the storage ring SPEAR as a function of the electron beam energy.

Fig. 12 Values for the mean-free-path of an electron in various solids as a function of the electron's kinetic energy (Ref. 14).

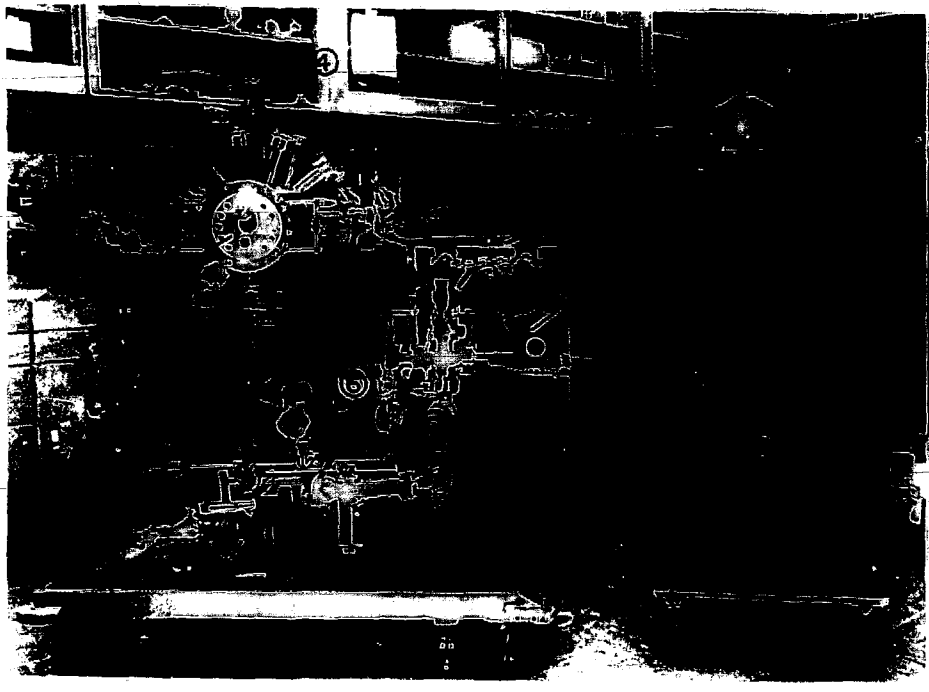

XBB 784-4575A

Figure 1

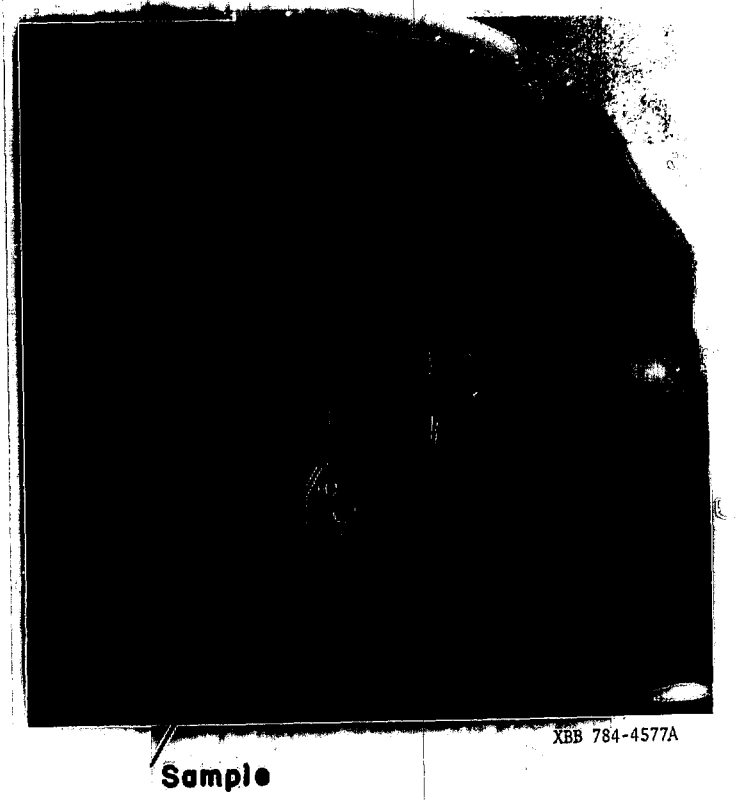

Figure 2

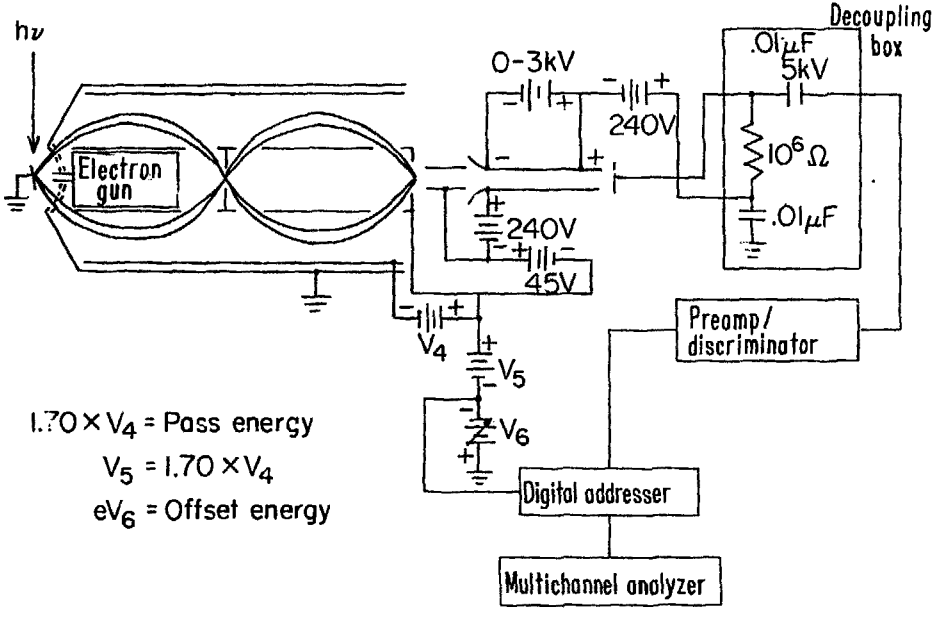

Figure 3

XBL 784-2492

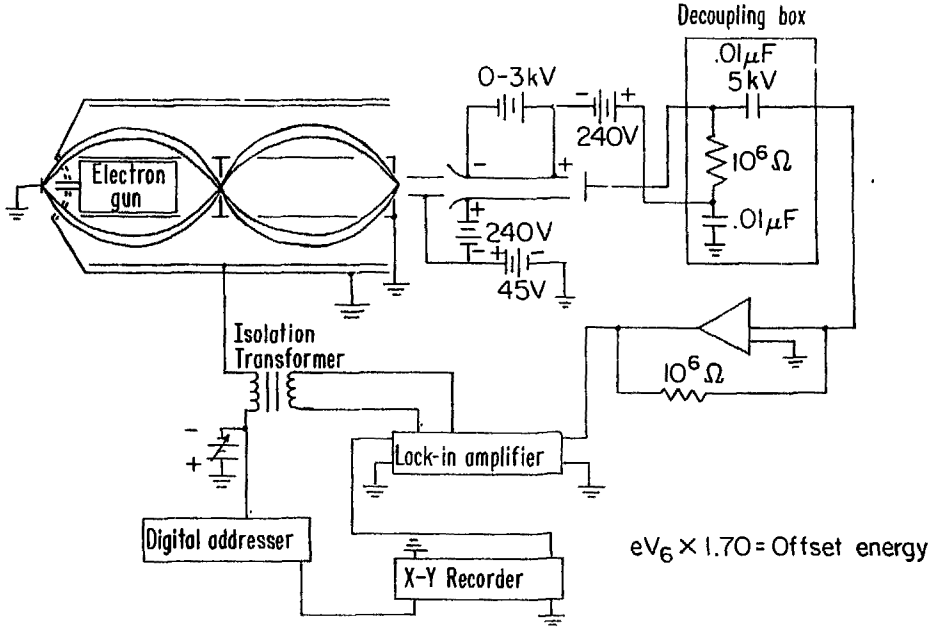

Figure 4

XBL 784-2493

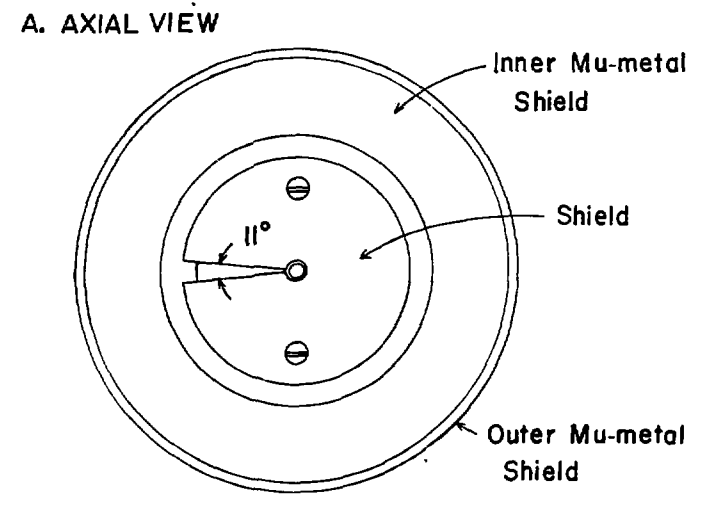

XBL 784-7992

Figure 5

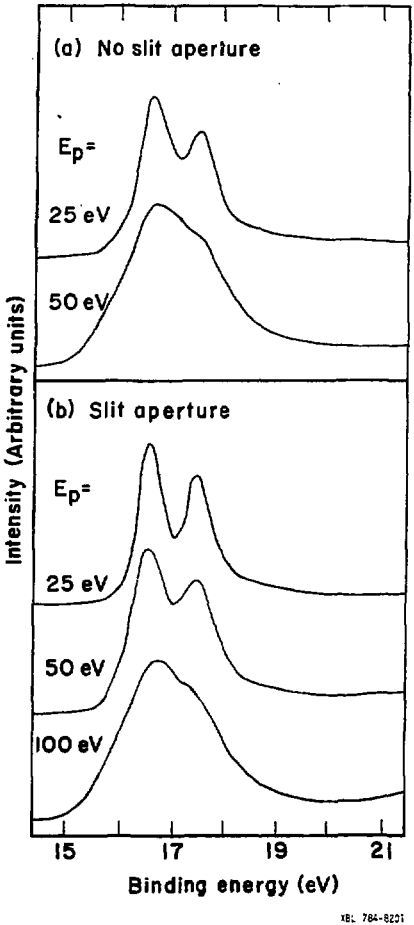
(a) No slit aperture
E_p=
25 eV
50 eV
(b) Slit aperture
E_p=
25 eV
50 eV
100 eV
Intensity (Arbitrary units)
15
17
19
21
Binding energy (eV)
XBL 784-8201

Figure 6

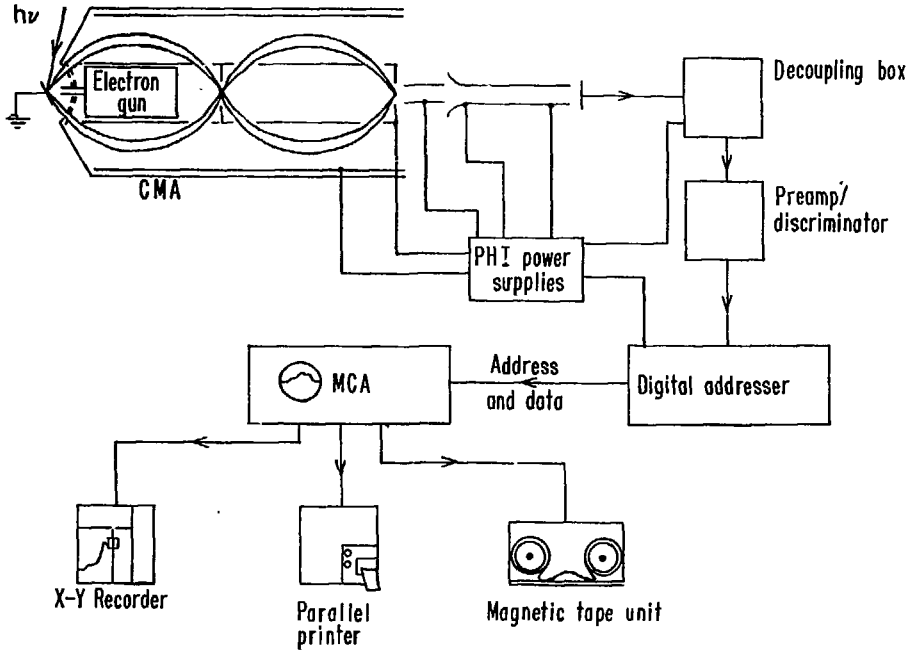

Figure 7

XBL 784-2494

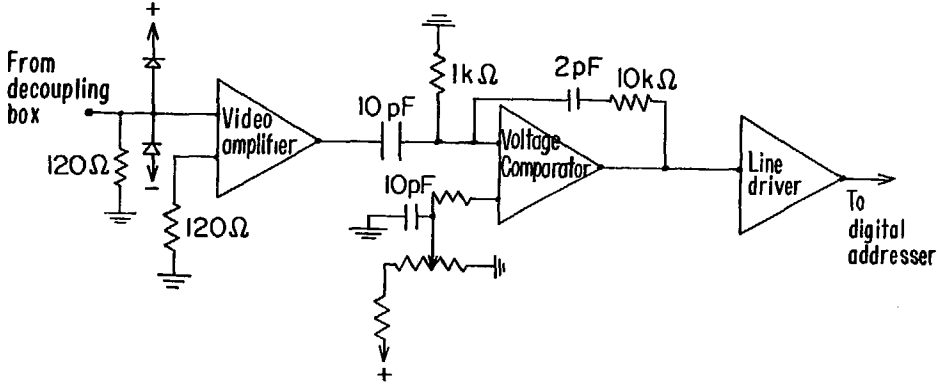

Figure 8

XBL 784-2491

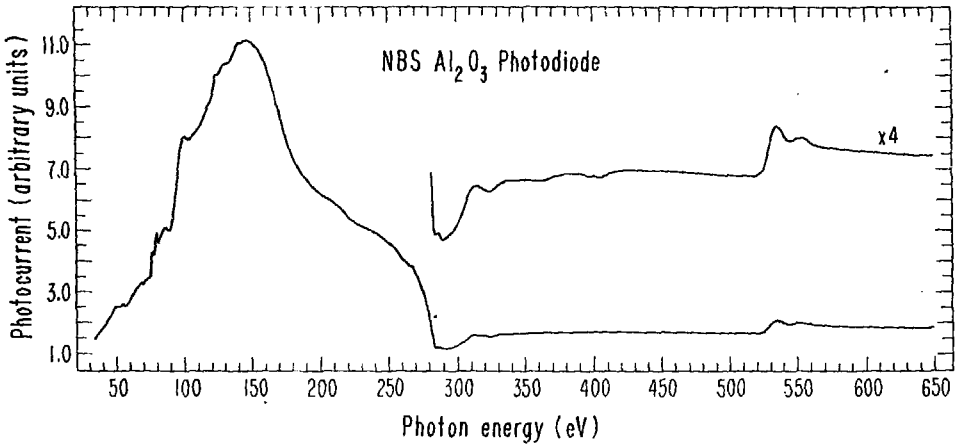

XBL 775-8634A

Figure 9

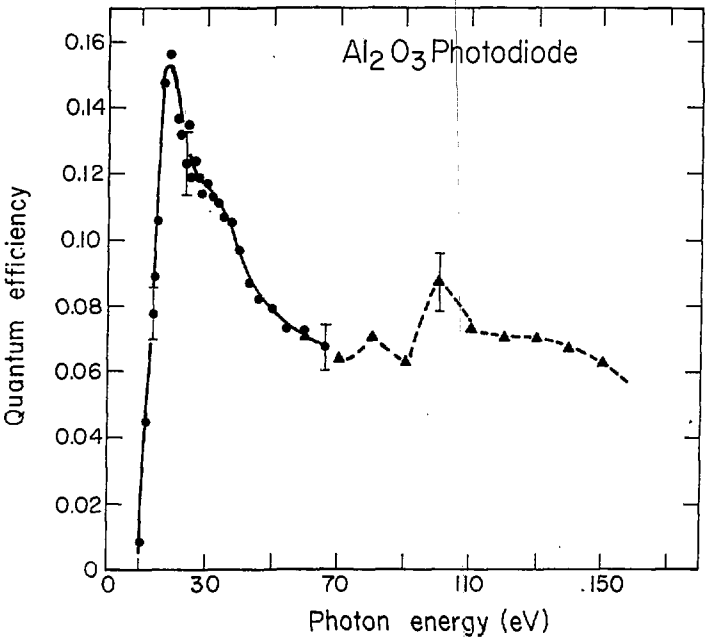

Figure 10 XBL 775-1019

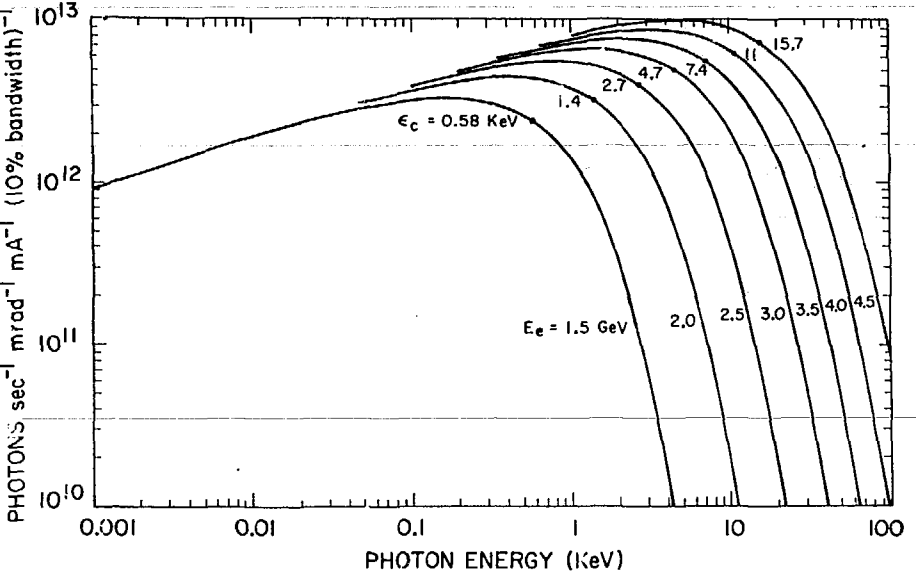

XBL 776-9334

Figure 11

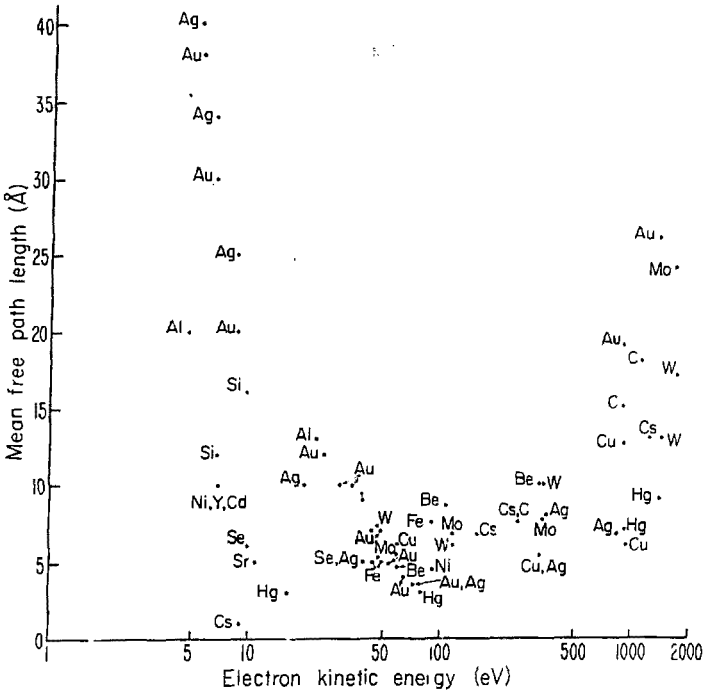
Mean free path length (Å)
Electron kinetic energy (eV)
0
5
10
15
20
25
30
35
40
5
10
50
100
500
1000
2000
Ag
Au
Al
Si
Ni,Y,Cd
Se
Sr
Cs
Hg
Ag,Au
Al
Au
Si
Ag
Au
Ni
Se,Ag
Fe
Mo
W
Cu
Be
Au,Ag
Hg
Cs,C
Ag
Mo
Cs
Be
W
Cu,Ag
Au
C
W
Mo
Au
C
Cs
W
Cu
Hg
Ag
Hg
Cu

Figure 12

III. ANGLE-RESOLVED PHOTOEMISSION FROM Cu SINGLE CRYSTALS IN THE PHOTON ENERGY RANGE 32 to 200 eV

A. Introduction

Angle-resolved photoemission (ARP) from single crystals has previously been reported in the ultraviolet [UPS, $h\nu \leq 40$ eV] (1) and x-ray [XPS, $h\nu \geq 1000$ eV] (2,3) photoemission regions. In these two regimes, significantly different information is contained in the experimentally observed photoelectron energy distribution (PED's). For UPS energies the PED's obtained by exciting valence electrons display structure characteristic of the energy distribution of the joint (initial and final) density of states; here, the three step model of photoemission (4), including strict energy and wavevector conservation during the excitation process, has been able to describe the experimental situation quite well. On the other hand, angle-resolved PED's observed at XPS energies basically depend on the symmetry properties of the initial states (1,2, and Chapter V). In this case, final-state band structure effects are weak, and the experimental spectra are well described by the initial density of states, modulated by an angle-dependent matrix element.

As of this writing, few ARP studies (5,6) have been performed in the transition region between UPS and XPS, namely the spectral range 40 to 1000 eV, due to a deficiency of suitable photon sources. The advent of electron storage rings, coupled with the development of new monochromators (7) is, however, rapidly making this region of the spectrum available for use. In this chapter, ARP studies of Cu single crystals in the photon energy range 32-200 eV are reported; these studies represent the first such investigations to be performed in this

energy range, and were conducted at SSRL (8), which is located on the electron storage ring SPEAR. In section B, we shall discuss angle-resolved normal-photoemission results obtained from the three low-Miller-index crystal faces of copper, i.e., the (001), (110), and (111) faces. Normal emission represents a particularly simple case theoretically, because the detailed relationship between $\vec{q}$, the wavevector of the electron inside the crystal, and $\vec{p}$, the wavevector outside the crystal, need not be considered explicitly; this results since for normal emission electron refraction at the surface is zero, and the propagation direction of the electron inside the crystal is therefore the same as that outside. Utilizing this simple observation, it will be demonstrated how the various peak positions in the spectra reported in this chapter can be related to the initial-state bulk band structure of copper using a direct transition model for the photoemission process.

We shall in section C shift our attention from normal emission and treat the problem of non-normal emission with particular emphasis on the matching conditions at the surface. We will show that simple free-electron matching conditions, as proposed by Mahan in 1970 (9), serve as an adequate first approximation for the calculation of electron refraction angles.

B. Normal Emission

B.1 Experimental

The experimental geometry used in these studies is shown in Fig. 1. The monochromatic photon beam was incident on a Cu single crystal which was positioned at the focal point of a PHI analyzer modified for ARP

studies as discussed in Chapter II. The electric field vector, $\vec{E}$, of the incident radiation lay in the plane defined by the photon beam and the propagation direction of the electron accepted by the analyzer. Its orientation with respect to the crystalline axes of the various samples employed is shown in Figs. 2 and 3. The fourfold cubic axes [100], [010], and [001] have been chosen as the frame of reference (x,y,z), and the orientation of the $\vec{E}$ vector and the detector is described in terms of the polar (θ) and azimuthal (ϕ) angles; this is summarized in Table I. The position of the x-ray beam and the detector were fixed relative to each other with the x-ray Poynting vector, $\vec{E}$ vector, and the detector acceptance axis lying in the horizontal plane. The Cu crystals were prepared and cleaned as described in Chapter II. The energy resolution of the electron energy analyzer was less than 0.2 eV, and the monochromator resolution varied from 0.01 eV ($h\nu$ = 32 eV) to ~0.50 eV ($h\nu$ = 250 eV).

B.2 Experimental Results

Cu(110)

Valence band spectra obtained in normal emission from Cu(110), as a function of the incident photon energy, are shown in Fig. 4. The most striking feature in these spectra is the intense peak in the "s - p" band region between the Fermi energy (E_F) and *ca.* 2 eV binding energy (E_B), which appears for 43 eV $\leq h\nu \leq$ 52 eV. In contrast to previously published Cu spectra (5) this peak is completely new and initially quite surprising. The intensity of this peak is comparable to that of the "d" band between 2 eV and 5.5 eV binding energy. In addition, it

shows strong dispersion, varying from E_B = 0.4 eV at hν = 43 to E_B = 1.7 eV at hν = 52 eV. The "s - p" band intensity vanishes in the energy range 70 eV ≤ hν ≤ 120 eV and shows another maximum near hν = 140 eV; at hν = 160 eV, it again diminishes in intensity. The "d" band region of the spectrum also exhibits strong changes in both peak positions and intensities. The width of the d-band narrows from ∿2.5 eV full-width-half-maximum (FWHM) at low photon energies to ∿1.5 eV FWHM in the range 70 eV ≤ hν ≤ 120 eV, then broadens to ∿2.5 eV FWHM at the highest photon energies utilized.

Cu(001)

Experimental PED's observed in normal photoemission from the valence band of Cu(001), as a function of the excitation energy, are shown in Fig. 5. The most interesting changes in these spectra occur in the photon energy range 70 to 160 eV. At hν = 70 eV, a new peak, at *ca.* 5 eV E_B, appears in the Cu spectrum; this peak grows in intensity and shifts in binding energy by ∿0.3 eV as the photon energy is raised to 110 eV, and then diminishes in intensity as the photon energy is increased further, until it vanishes at hν = 160 eV. The "s - p" band reaches maximum intensity in this photon energy region as well; it is very weak at low photon energies, showing maximum intensity at hν ∿ 80 eV, and then decreasing in strength again at higher photon energies.

Cu(111)

Fig. 6 shows the valence band spectra acquired in normal emission from Cu(111) as a function of the energy of the incident radiation. In this case, the most distinct variations in the ARP spectra occur between hν = 50 eV and hν = 100 eV. A feature at *ca.* 5 eV binding energy shows

a broad resonance in this photon energy range, reaching a maximum in intensity at $h\nu = 85$ eV. The "s - p" band, which is very weak at $h\nu = 45$ eV, attains its maximum intensity in this energy range as well.

Finally, it should be noted that distinct differences exist between spectra taken at the same photon energy but along different directions, as is evidenced by comparing Figs. 4-6; note in particular the opposing changes in the width of the d-band for the three directions as the photon energy is swept from 32 to 160 eV.

B.3 Discussion

The theoretical aspects of photoemission from a solid have been treated by a number of authors (9-15), and several excellent review papers exist (1,4,14). Briefly, in the independent-particle approximation adopted here, the photocurrent emanating from a sample, as a result of the interaction with light of frequency ν, is given by:

$$N(E, h\nu) \propto \int_{BZ} d^3k_i \sum_{i,f} |\langle \phi^f(\vec{r}) | \vec{A}\cdot\vec{p} | \phi^i(\vec{r}) \rangle|^2 \delta(\vec{k}_f - \vec{k}_i - \vec{k}_{h\nu} - \vec{G}) \times$$
$$\times \delta(E_f(\vec{k}_f) - E_i(\vec{k}_i) - h\nu) \, \delta(E - E_i(\vec{k}_i)) \, . \qquad (1)$$

Here $\phi^i(\vec{r})$ and $\phi^f(\vec{r})$ are electron wavefunctions of an initial state of wavevector $\vec{k}_i$ and energy E_i and a final state of wavevector $\vec{k}_f$ and energy E_f, respectively. The δ-functions represent the requirements of energy and wavevector (momentum) conservation in the excitation process, with the latter arising from a sum over reciprocal lattice vector, $\vec{G}$. $\vec{k}_{h\nu}$ is the photon wavevector which for radiation in the energy range of interest here, namely 32 to 250 eV, is very small ($k_{h\nu} \leq 0.07$ in units

of $\frac{2\pi}{a}$, where a is the lattice constant of copper) and therefore will be neglected hereafter. In the reduced zone scheme, electronic transitions in this model are vertical (see Fig. 7), and hence this picture of photoemission is referred to as the Direct Transition Model.

In order to evaluate Eq. (1), i.e., generate theoretical PED's, detailed knowledge of both the initial and final state band structures and wavefunctions is required. While such information is available for the initial state, in the form of theoretical band structure calculations (15), the description of the final state represents a major problem, because such calculations are in general unavailable. For this reason, two assumptions concerning the nature of the final state have been made. First, it has been assumed that the free-electron dispersion relationship (16),

$$E_f(\vec{k}) = (\hbar^2/2m)|\vec{k} + \vec{G}|^2 + \beta \ , \qquad (2)$$

where $\vec{k}$ is the momentum of the electron in the reduced zone scheme and β is a constant used to adjust the zero of the free-electron bands to coincide with the bottom of the 4s-band in Cu, adequately describes the final-state band structure in the region of interest; this relationship is shown in Fig. 8. Secondly, since the main concern here is with peak positions and not intensities, secondary Mahan cones (9) will be neglected, i.e., the final state is taken to be composed of a single plane wave.

This latter point deserves a little more discussion. In general, in a bulk interband optical transition an electron is excited into a state whose wavefunction

$$\phi_f(\vec{r}) = \sum_{\vec{G}} a_{\vec{G}} \exp[i(\vec{k} + \vec{G})\cdot\vec{r}] \qquad (3)$$

has plane wave components going in many different directions. The intensity in each of these directions is determined by the respective coefficients $a_{\vec{G}}$ in equation (3). If the pseudopotential is relatively weak, as is the case for most transition metals, one term in this sum should dominate for low energy electrons (17), the term corresponding most nearly to that of the free-electron dispersion relationship [Eq. (2) and Fig. 8]. Therefore, most emission should occur in the associated direction (the Primary Mahan cone) and only weak emission will be observed in the other directions (Secondary Mahan cones) (9). It must be pointed out, however, that although it has been assumed that one plane wave component dominates the final state as far as the direction of propagation is concerned, the matrix element in Eq. (1) still depends on the entire sum in Eq. (3); this results because, even though the coefficient multiplying the other plane wave terms in Eq. (3) is small, the overlap integral between the initial state and these other components can be substantial. We shall, therefore, confine our attention to peak positions and shall make only general remarks concerning peak intensities.

With the above description of the final state, the constraints of energy and momentum conservation in u.v. photoemission greatly restrict the portion of the initial states in the Brillouin Zone (BZ) sampled in ARP. For example, consider emission in the [001] direction from a single crystal, as shown schematically in Fig. 9. Here an angular resolution of ±5° and the direct transition model discussed above have been assumed. The constraints of momentum conservation and the directionality of the photoelectron momentum vector ($\vec{q}$ must point toward the

detector) severely limit the amount of the BZ (to a section of a spherical surface) which can contribute to the photoemission spectrum. As the photon energy is changed the area in the first BZ which may give rise to emission (energy conservation must still be satisfied) also varies as illustrated in Fig. 9. Thus, variations in the ARP spectrum with energy or angle arise in this model because different parts of the first BZ are being sampled.

Calculations using Eq. (1), where the sum over $\vec{k}_f$ has been restricted to just those $\vec{k}_f$-values which can be observed and where constant matrix elements are assumed, have been performed by Wagner, *et al.* (18) for emission in the [001] and [111] directions and by Wehner and co-workers (19) for emission in the [110] direction. In both sets of calculations there is excellent agreement with all the major changes in structure occurring as functions of photon energy. The positions and overall widths of most of the peaks were reproduced well in the calculations, indicating that the assumption of constant matrix elements, at least for Cu, is a reasonable approximation at these low photon energies. (Janak, *et al.*, Ref. 20, arrived at the same conclusion, i.e., that the transition matrix elements for Cu can be assumed to be constant, in calculations of polycrystalline Cu photoemission spectra in the energy range 8 eV $\leq h\nu \leq$ 26 eV.) An example of the type of agreement obtained is shown in Fig. 10, where the results of a calculation for photoemission in the [110] direction at a photon energy of 45 eV are presented. As seen in the figure, the overall concurrence in peak positions and widths is very good; note, in particular, that the pronounced "s - p" resonance observed experimentally is predicted

by the calculations.

A more instructive way of viewing the results, however, is shown in Fig. 11. Here the experimental peak positions $E_{ex}(\vec{k})$ are compared with Burdick's (21) band structure of Cu. The locations of the experimental points in the figure were derived as follows. From the measured peak position, relative to E_F, the final state energy $E_f = E_{ex}(\vec{k}) + h\nu$ was calculated. The magnitude of the final state wavevector was then determined from the free-electron dispersion relationship $|\vec{q}| = (2mE_f/\hbar^2)^{1/2}$, where the zero of the free-electron scale was taken to be the bottom of the free-electron-like bands in Burdick's band structure. The relation $\vec{q} = \vec{k} + \vec{G}$ then yields $\vec{k}$ in the first BZ. Here we have made use of the fact that for normal emission the propagation direction of the electron inside the crystal is the same as that outside the solid, i.e., there is no surface refraction of the electron. The corresponding values of $E_{ex}(\vec{k})$ are plotted as bars in the figure. The horizontal scale at the bottom of each panel establishes a correspondence between the photon energy employed and the part of the BZ sampled, assuming an initial state of 3.5 eV (middle of the d-band).

Comparison of the experimental peak positions with Burdick's band structure in Fig. 11 reveals generally good agreement. In particular, the pronounced "s - p" band resonance for photoemission in the [110] direction at $h\nu = 45$ eV is fully explained in terms of bulk transitions arising from a well-defined part of the BZ [points near $\vec{k} = \frac{2\pi}{a}$ (-0.5, -0.5, 0.)]. The appearance of an s - p band at only certain photon energies is explained as well. Only when photoemission occurs in a part of the zone where a band exists near E_F is an s - p band observed,

e.g., for photoemission in the [111] direction at hν = 70 eV, states near L are sampled (see Fig. 6 and 11c). Finally, the variation in the width of the d-band is also easily understood in terms of the dispersion of the bands across the zone.

To illustrate further the direct relationship between photoemission spectra and the band structure for copper in this energy range, it is instructive to compare Fig. 5 and Fig. 11a. Both pertain to the [001] direction. Varying the photon energy from 32 eV up to 160 eV yields first a narrow peak, evolving into two widely-spaced peaks, then back into a relatively narrow peak (Fig. 5). But this is exactly as expected in going from Γ in the second zone through X to Γ in the third zone (Fig. 11a). The deviations in Fig. 11a between the experimental peak positions and the theoretical band structure are due almost entirely to the finite k-resolution. Calculated PED's, where the finite angular resolution of the measurements is included (18), do not show such large discrepancies between calculated and observed peak positions.

At this point a comment on a recent paper by Heimann, Neddermeyer, and Roloff (22) is in order. These authors have reported angle-resolved normal photoemission spectra from Cu(110) at Ne I (16.88 eV) and He I (21.2 eV) energies, and have explained their results in terms of a one-dimensional density-of-states along the Γ-K-X direction. The apparent lack of conservation of the crystal momentum component perpendicular to the surface was attributed to surface photoemission from bulk-like initial states (which extend to the surface) to free-electron-like final states in the vacuum. This interpretation is, however, very puzzling in light of the preceding discussion, where direct transitions,

i.e., $\vec{k}$-conserving transitions, from bulk bands were found to account for all the observed structure in the PES spectra obtained from Cu(110) in the energy range 32 eV $\leq h\nu \leq$ 160 eV. The proposed explanation is even more perplexing when the mean-free-path (λ) of a 20 eV electron in copper ($\lambda \sim$12Å, Ref. 23) is considered; approximately ten atomic layers contribute to the PES spectra obtained from a Cu(11C) crystal at the photon energies employed by Heimann, and one would therefore expect bulk photoemission, characterized by strict $\vec{k}$-conservation, to make the dominant contribution to the spectra. For this reason, an attempt at reinterpreting the data of Heimann and co-workers utilizing the direct transition model described above has been made.

The results of these calculations are summarized in Fig. 12, where a comparison of the experimental peak positions observed by Heimann, *et al.* with Burdick's band structure of copper is shown. Because the final states at 16.88 eV and 21.2 eV lie almost symmetrically around X and the bands are flat in this area, the same peak positions are predicted. In the figure the same labels as used in Ref. 22 for the data points are employed. Excellent agreement is found between peaks f, d, a, and g and the band structure. Only peak b, the weakest experimental structure observed, does not coincide with a band around X. The direct-transition model used here predicts the observed peak positions better than the one-dimensional density of states (ODDS) calculation of Heimann, *et al.* In particular, no shift in Burdick's bands is needed in order to match experimental and theoretically-predicted peak positions, while a 0.3 eV shift had to be assumed by Heimann and co-workers. Other discrepancies between the theoretical ODDS calculations of Ref.

22 and experiment lie in the prediction of a shoulder on peak a and especially of the width of peak d. Experimentally, and according to Fig. 12, peak d is confined to $E_B < 2.5$ eV, while the ODDS predicts that it extends to $E_B \sim 3.0$ eV, merging into another peak (c) at $E_B = 3.2$ eV; this shift is not observed experimentally. It should be noted that weak structures similar to peak b may arise from electrons originating at $\vec{k}$-points where the bands are flat (e.g., $k_x = k_y = -0.4$ in Fig. 12) which reach the detector via scattering at surface irregularities (24) or surface umklapp processes.

In their direct-transition calculation Heimann and co-workers used the model proposed earlier by Christensen and Feuerbacher (25). In this model *all final states* with reduced wavevectors $\vec{k}$ along the Γ-K-X direction are allowed, while in the model described above an additional condition has to be satisfied, namely, that $\vec{q} = \vec{k} + \vec{G}$ points into the analyzer. The fact that the calculations performed using this latter model agree with experiment thus indicates that the final state Bloch-functions in Cu consists of one strong plane wave component (i.e., one $\vec{G}$-vector dominates) at these low energies.

To close this subsection a brief comment on photoemission cross sections and the reason why certain bands, in particular the band between 6 and 9 eV binding energy which exists in all three directions studied (see Fig. 11), do not give rise to peaks in the photoemission spectrum is appropriate. From atomic data at u.v. (26) and x-ray (27) energies, we can estimate that the photoemission cross section of 4s electrons is almost an order of magnitude smaller than that for 3d electrons in the photon energy range utilized here. It follows

therefore, that only bands which have a significant admixture of d-character will give rise to peaks in the photoemission spectrum. Hence, the band described above, which a tight-binding calculation (19) shows to be predominantly "s" in character, is not expected to be observed and in fact is not. Conversely, all the peaks observed do indeed correspond to bands having substantial d-character.

C. Non-Normal Emission

For non-normal emission the relation between $\vec{q}$ and $\vec{p}$ must be considered explicitly, as due to the presence of a potential at the surface, the propagation directions of the electron inside and outside the crystal need not be the same. With a simple free-electron description of the final state and the assumption of specular boundary conditions, the following relationships between $\vec{q}$ and $\vec{p}$ obtain (9):

$$\vec{p}_{\parallel} = \vec{q}_{\parallel} \quad ;$$
$$(\hbar^2/2m^*)\,|\,q_{\perp}\,|^2 = (\hbar^2/2m)\,|\,p_{\perp}\,|^2 + V_o \quad . \tag{4}$$

Here $p_{\perp}$ and $q_{\perp}$ are the components of $\vec{p}$ and $\vec{q}$ perpendicular to the surface, while $\vec{p}_{\parallel}$ and $\vec{q}_{\parallel}$ are the parallel components. V_o denotes the inner potential, the energy difference between the zero of energy in the crystal and the vacuum level (13.8 eV for Cu). The effective mass of the electron inside the crystal is represented by m^*, whereas the mass of the electron outside the crystal is given by m (the free-electron value). Solving these equations for θ, the angle between the emerging electron's propagation direction and the surface normal $\hat{n}$, we obtain:

$$\theta = \arcsin[(m^*(E + V_o)/mE)^{\frac{1}{2}}\sin\theta'] \quad , \tag{5}$$

where θ' is the angle between the photoelectron's propagation direction and $\hat{n}$ inside the crystal, and E is the measured kinetic energy of the detected electron. The validity of Eq. (5) in photoemission has been assumed in the past for $m^* = m$, but has never been tested.

To determine the accuracy of expression (5) for describing non-ideal systems, ARP experiments have been performed on (001), (110), and (111) Cu single crystals, in all cases at a photon energy of 45 eV and in a [110] emission direction (for (001) and (111) crystal faces, the [110] directions fall at 45° and 35° away from the normal, respectively). These particular experiments were chosen due to the presence of an extremely sharp resonance in the s - p band of Cu at this energy (see Fig. 4), which is very sensitive to the exact portion of the BZ being sampled. This peak (which shall hereafter be referred to as the band-six resonance) arises only through transitions from the 6^{th} valence band, which goes steeply through E_F between Γ and K as shown in Fig. 11b.

In Fig. 13 the results of this study are presented. Here the relative area under the band-six resonance is plotted as a function of the emission angle (α), measured from the sample normal. Results obtained from (110) crystals, Figs. 13b and 13d, show that the maximum in intensity of the band-six peak occurs for normal emission, i.e., along the [110] direction. The difference in the detailed shapes of the two curves arises from the fact that the azimuthal orientation of the two crystals relative to the $\vec{E}$ vector of the incident radiation differs by 90° (see insets in figure and Ref. 28). Inspection of Figs. 13a and 13c shows that the maximum in intensity is shifted from the bulk [110]

crystalline direction for emission from (001) and (111) single crystals, indicating refraction of the photoemitted electron at the crystal-vacuum interface. The resulting refraction angles are ∿15° and ∿12° for emission in the [110] direction from a (001) and (111) crystal, respectively.

Comparison of these refraction angles with those calculated using Eq. (5), which yields values for $(\theta - \theta')$ of 10° and 7° for emission in the [110] direction from (001) and (111) single crystals (here $m^* = m$ has been assumed), respectively, shows that fair agreement is obtained. There is, however, a discrepancy of ∿5°, the calculated values being larger than those observed experimentally, and this discrepancy is considerably larger than the estimated 2° uncertainty associated with the measurements. Several possible explanations for this disagreement can be suggested. First, the magnitude of the inner potential used in the calculations may have been wrong. If the assumption that $m^* = m$ is made and the measured values of θ are used to determine V_o from Eq. (5), one finds that V_o would have to be on the order of 18-20 volts to account for the large refraction angles. This is unrealistic, however, because the inner potential for excited electrons should be less than that for valence electrons, due to the decreased magnitude of the exchange-correlation potential with increasing electron energy (29). To ascertain whether the calculated refraction angles are sensitive to the form of V_o, as suggested by Gartland and Slagsvold (30) for 5 eV photoelectrons, the step potential was replaced by a softer potential of the form $V(z) = a/(c + z)$, where a and c are constants and $z > 0$ measures the distance of the photoelectron from the surface; in this way, we may roughly account for the image charge induced in the metal

(31, 32) by the ejected electron. The calculated refraction angles as a function of a and c revealed, however, that for 40 eV electrons, there is no significant difference in refraction angles caused by the two potentials.

If the position is taken that V_o is fixed at 13.8 eV for copper (which is certainly an upper limit for hot electrons), two possible reasons remain for the unexpectedly large refraction angles. Since $\hbar^2p^2/2m$ is effectively a measured quantity, and V_o is taken as fixed, the data can be fit by Eq. (5) only if m^* is different than the free-electron value. An effective mass of $m^* = 1.15m$ yields $\theta = 45.5°$ and 61.7° for the (111) and (001) faces, respectively. That m^* may assume a value other than m for the final state photoelectron is plausible, since the nominally observed final state for $\vec{q} = \frac{2\pi}{a}(-0.5,-0.5,0)$ and $\vec{G} = \frac{2\pi}{a}(2,2,0)$ is degenerate with another band of the same symmetry arising from $\vec{G} = \frac{2\pi}{a}(0,0,2)$. The perturbation should be small (the two bands mix through the Fourier potential component for $\vec{G} = \frac{2\pi}{a}(2,2,2)$); however, the interaction may be large enough to affect the group velocity of the hot electron, i.e., induce an effective mass different from the free-electron value. Furthermore, Moruzzi and co-workers (33) find that a value of $m^* = 1.08m$ for hot electrons ~20 eV above E_F allows a good fit of their calculated Cu band structure to photoemission data. It thus seems plausible that an increased effective mass is responsible for the large refraction angles.

Finally, the other possible cause for large refraction angles is surface roughness. In these experiments it was not possible to measure surface roughness on the (nearly) atomic scale that would be relevant

to this problem. It is not clear, however, exactly how surface roughness would affect the observed values of θ. In fact the effects on θ for all the geometries studied in the present work are expected to be model-dependent and quite small for plausible models (34). It seems very unlikely that an increase in θ by as much as 5° could arise from surface roughness. A more probable result of surface roughness is a spread in θ and in this connection, it should be noted that the band-six resonance persists over a larger range of angles for the off-normal geometries than would be expected from the normal-geometry photoemission experiments on the (110) face.

In summary, it has been shown for the first time that refraction of the photoelectrons at the solid-vacuum interface does occur and that the refraction angle is somewhat larger than that expected in a simple free-electron picture. This latter result can not be uniquely explained; however, from the data it appears plausible that an increased effective mass of the hot electron is responsible for the unexpectedly large refraction angles.

REFERENCES

1. For a recent review see B. Feuerbacher and R. F. Willis, J. Phys. C9, 169 (1969).
2. R. J. Baird, L. F. Wagner, and C. S. Fadley, Phys. Rev. Lett. 37, 111 (1976).
3. F. R. McFeely, J. Stöhr, G. Apai, P. S. Wehner, and D. A. Shirley, Phys. Rev. B14, 3273 (1976); G. Apai, J. Stöhr, R. S. Williams, P. S. Wehner, S. P. Kowalczyk, and D. A. Shirley, Phys. Rev. B15, 584 (1977); P. S. Wehner, J. Stöhr, G. Apai, F. R. McFeely, and D. A. Shirley, Phys. Rev. Lett. 38, 169 (1977).
4. For a recent review see D. E. Eastman in Vacuum Ultraviolet Radiation Physics, Edit. E. E. Koch, R. Haensel, and C. Kunz, (Pergamon, Vieweg 1974), p. 417.
5. J. Stöhr, G. Apai, P. S. Wehner, F. R. McFeely, R. S. Williams, and D. A. Shirley, Phys. Rev. B14, S144 (1976).
6. J. Stöhr, P. S. Wehner, R. S. Williams, G. Apai, and D. A. Shirley, Phys. Rev. B, to be published.
7. For a description of the monochromator used in the studies reported in this chapter see F. C. Brown, R. Z. Bachrach, S. B. M. Hagström, N. Lien, and C. H. Pratt in Ref. 4, p. 785.
8. H. Winick in Ref. 4, 776.
9. G. D. Mahan, Phys. Rev. B2, 4334 (1970).
10. J. B. Pendry, Surface Science 57, 679 (1976).
11. C. Caroli, D. Lederer-Rozenblatt, B. Roulet, and D. Saint-James, Phys. Rev. B8, 4552 (1973).
12. N. W. Ashcroft in Ref. 4, p. 555.

13. W. L. Schaich and N. W. Ashcroft, Phys. Rev. B3, 2452 (1971).

14. G. D. Mahan in Electron and Ion Spectroscopy of Solids, Edit. W. Dekeyser, J. Vennik, and L. Fiermans, to be published.

15. Many band structure calculations exist for copper: An-Ban Chen and Benjamin Segall, Phys. Rev. B12, 600 (1975); B. Segall, Phys. Rev. 125, 138 (1963); see also Refs. 20, 21, and 33.

16. See for example L. Pincherle, Electronic Energy Bands in Solids (MacDonald, London, 1971), pp. 104-108.

17. N. J. Shevchik and D. Liebowitz, to be published.

18. L. F. Wagner, Z. Hussain, and C. S. Fadley, Solid State Commun. 21, 257 (1977).

19. The LCAO interpolation scheme of Hodges, Ehrenreich, and Lang was employed to generate the initial state band structure for copper in our calculations. For a description of this interpolation scheme see L. Hodges, H. Ehrenreich, and N. D. Lang, Phys. Rev. 152, 505 (1966). The various parameters used to generate the copper band structure are: E_c = .55075, E = -0.1, α = 0.015515, A_1 = 0.01828, A_2 = 0.00681, A_3 = 0.00923, A_4 = 0.01295, A_5 = 0.00262, A_6 = 0.00909, V_{111} = 0.125, V_{200} = 0.176, B_1 = 0.4126, B_2 = 1.0, B_3 = 1.0, C = 0.0, Δ = -0.00445.

20. J. J. Janak, A. R. Williams, and V. L. Moruzzi, Phys. Rev. B11, 1522 (1963).

21. G. A. Burdick, Phys. Rev. 129, 138 (1963).

22. P. Heimann, H. Neddermeyer, and H. F. Roloff, Phys. Rev. Lett. 37, 775 (1976).

23. I. Lindau and W. E. Spicer, J. Electron Spectrosc. 3, 409 (1974); C. R. Bundle, Surf. Sci. 48, 99 (1975); I. Lindau, P. Pianetta, K. Y. Yu, and W. E. Spicer, J. Electron Spectrosc. 8, 487 (1976); D. T. Ling found the escape depth of Cu(110) to be shortest around 80 eV. (Private communication)

24. E. Dietz, H. Becker, and U. Gerhardt, Phys. Rev. Lett. 36, 1397 (1976).

25. N. E. Christensen and B. Feuerbacher, Phys. Rev. B10, 2349 (1974).

26. S. Suzer, P. R. Hilton, N. S. Hush, and S. Nordholm, J. Electron Spectrosc. 12, 357 (1977). The measured photoemission cross section for 3d electrons in atomic zinc is ~18 times that for 4s electrons at HeII ($h\nu$ = 40.8 eV).

27. J. H. Scofield, J. Electron Spectrosc. 8, 129 (1976). The calculated photoemission cross section for 3d electrons in copper is 10 times that for 4s electrons at $h\nu$ = 1486.6 eV (AlKα x-rays).

28. For discussion of polarization effects in photoemission form solids see: J. E. Rowe, G. Margaritondo, and H. Kasper, Nuovo Cimento 38B, 226 (1977); J. A. Knapp and G. J. Lapeyre, Nuovo Cimento 39B, 696 (1977); J. Hermanson, Solid State Commun. 22, 9 (1977).

29. L. Hedin and B. I. Lundquist, J. Phys. C4, 2064 (1971).

30. P. O. Gartland and B. J. Slagsvold, Phys. Rev. B12, 4047 (1975).

31. R. Ray and G. D. Mahan, Phys. Lett. 42A, 301 (1972).

32. M. Sunjic and G. Toulouse, Solid State Commun. 11, 1629 (1972).

33. V. L. Moruzzi, P. M. Marcus, and J. A. Knapp, to be published.

34. C. S. Fadley, Progress in Solid State Chemistry 11, 265 (1976).

Table I. Experimental geometry for photoemission from single crystals of Cu.

	Cu[001]^b	Cu[111]^b	Cu[110]
$\vec{E}$ vector^a	θ = 27.5°	θ = 27.5°	θ = 62.5°
	ϕ = 45°	ϕ = 45°	ϕ = 45°
Detector^a	θ = 0°	θ = 54.5°	θ = 90°
	(along z axis)	ϕ = 45°	ϕ = 45°

a) All values have been rounded to the nearest 0.5°.

b) Electrons were taken off normal to the (001), (111), and (110) crystal faces, respectively.

FIGURE CAPTIONS

Fig. 1 Experimental geometry for angle-resolved photoemission studies of Cu single crystals. A cylindrical-mirror analyzer modified for angle-resolved measurements as described in Chapter II was employed. The angular resolution was ±6° in the horizontal plane and ±4° in the vertical plane.

Fig. 2 Experimental orientation of the x-ray beam, $\vec{E}$ vector, and detector relative to the fourfold cubic crystalline axes x,y, and z for the (111) and (001) Cu crystals. The polar (θ) and azimuthal (ϕ) angles define the orientation of the $\vec{E}$ vector in the coordinate system x,y, and z. The crystal could be rotated about a vertical axis. The x-ray beam, $\vec{E}$ vector, and detector positions were fixed in the laboratory frame of reference and lay in the horizontal plane.

Fig. 3 Experimental orientation of the x-ray beam, $\vec{E}$ vector, and detector relative to the fourfold cubic crystalline axes x,y, and z for the (110) Cu crystal. The notation is the same as that used in Fig. 2.

Fig. 4 Photoemission energy distributions obtained from a Cu(110) single crystal in the photon energy range $32 \leq h\nu \leq 160$ eV. Only electrons emitted normal to the surface were analyzed.

Fig. 5 Photoemission energy distributions obtained from a Cu(001) single crystal in the photon energy range $32 \leq h\nu \leq 200$ eV. Only electrons emitted normal to the surface were analyzed.

Fig. 6 Photoemission energy distributions obtained from a Cu(111) single crystal in the photon energy range $32 \leq h\nu \leq 200$ eV. Only electrons emitted normal to the surface were analyzed.

Fig. 7 a) Interband transition pictured in the reduced zone scheme assuming the direct transition model discussed in text, and neglecting the wavevector of the incident radiation. In this framework the electronic transition is vertical.

b) Interband transition pictured in the extended zone scheme showing involvement of a reciprocal lattice vector, $\vec{K}$. Note that the transition is now diagonal.

Fig. 8 Energy bands along high symmetry directions for a free-electron in the copper lattice (an fcc lattice).

Fig. 9 a) (010) projection of the three-dimensional Brillouin Zone (BZ) of copper.

b) Photoemission at $h\nu = 32$ eV along the [001] direction assuming an angular resolution of ±5° and free electron final states. Only a small fraction of the first BZ (a section of a spherical surface) can give rise to photoemission ($\vec{q}$ vectors) into the detector due to momentum conservation.

c) Photoemission at $h\nu = 90$ eV along the [001] direction.

d) Photoemission at $h\nu = 200$ eV along the [001] direction. Note that as $h\nu$ is increased different portions of the first BZ are sampled.

Fig. 10 Comparison of a calculation (dashed curve) for photoemission in the [110] direction at a photon energy of 45 eV and an angular resolution of ±5° to the experimentally observed spectrum (solid line). The calculation was convoluted with a 0.5 eV FWHM Gaussian function to simulate experimental resolution.

Fig. 11 Comparison of experimental peak positions with Burdick's band structure of Cu [21] for the three directions investigated. The inset at the top of each panel shows the propagation direction of the photoelectron in the extended zone scheme. The bottom inset establishes a correspondence between photon energy and the part of the Brillouin zone sampled; a) Cu[001]; b) Cu[110]; c) Cu[111]. Note the different scales.

Fig. 12 Burdick's band structure for copper [21] along the U-X-U direction (solid lines). The filled triangles are Heimann's [22] experimental peak positions.

Fig. 13 Relative area under the band-six resonance peak compared to the total Cu valence band area (as a function of the emission angle θ, measured from the sample normal) for $h\nu$ = 45 eV. The azimuthal orientation of the crystalline axes defining the detection plane for the data presented in Fig. 14a and 14c were equivalent to Fig. 14b and 14d (insets), respectively. The angular acceptance was ±5° and the energy resolution 0.2 eV.

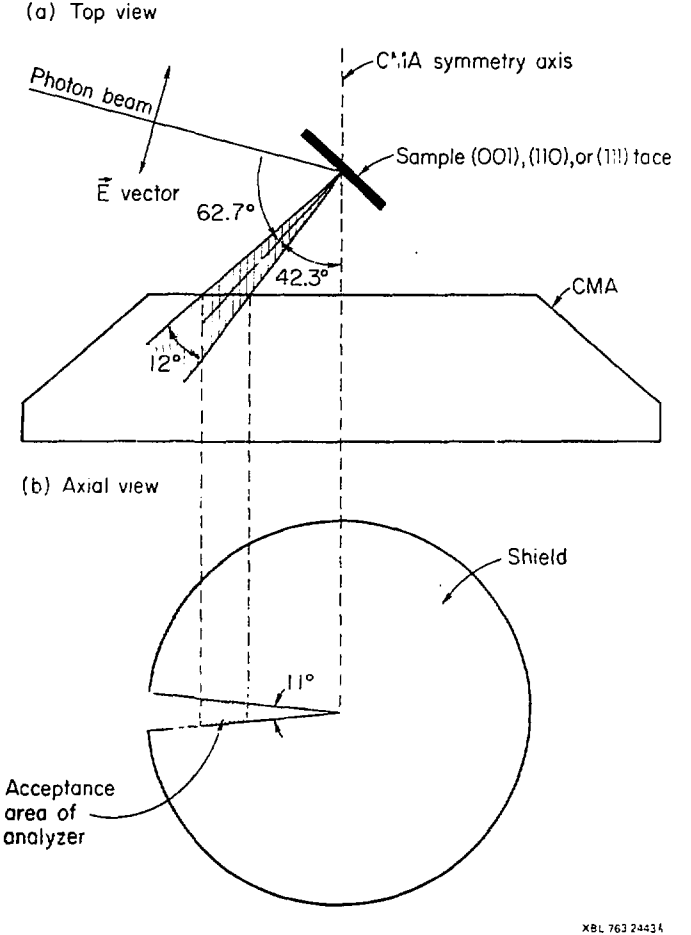
(a) Top view
CMA symmetry axis
Photon beam
Sample (001), (110), or (111) face
$\vec{E}$ vector
62.7°
42.3°
CMA
12°
(b) Axial view
Shield
11°
Acceptance area of analyzer
XBL 763 2443A

Figure 1

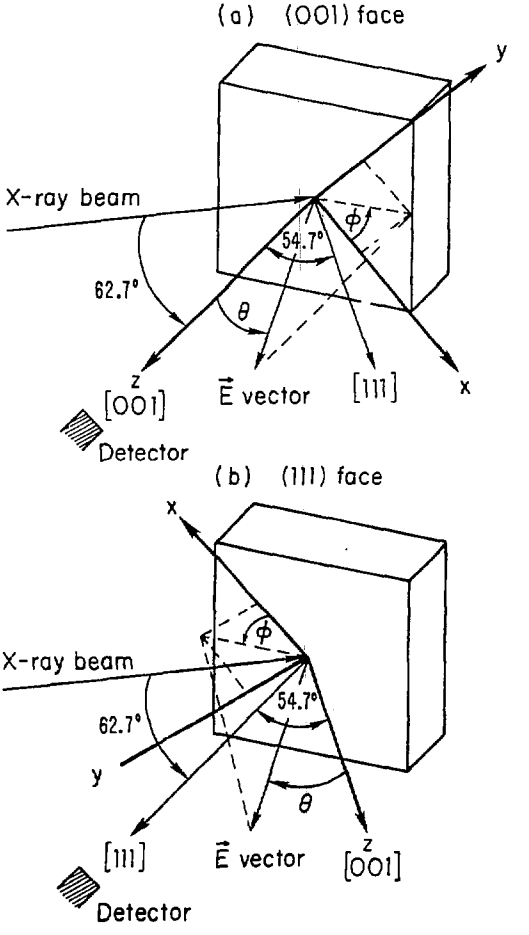

XBL 763-2526

Figure 2

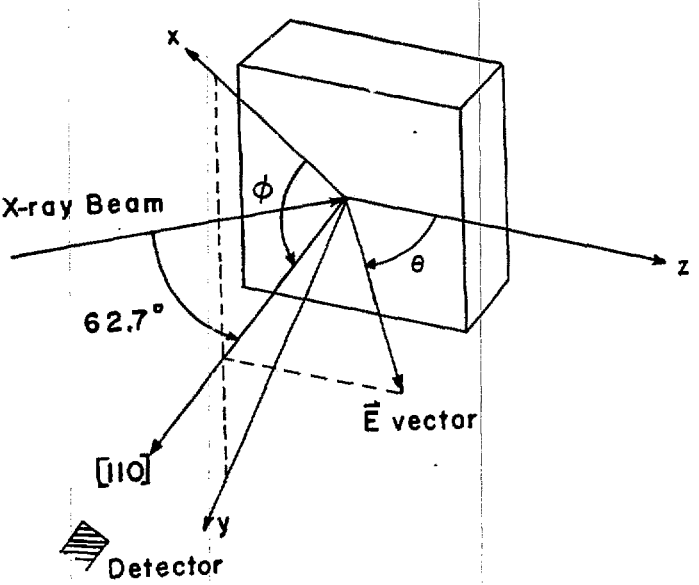

Figure 3

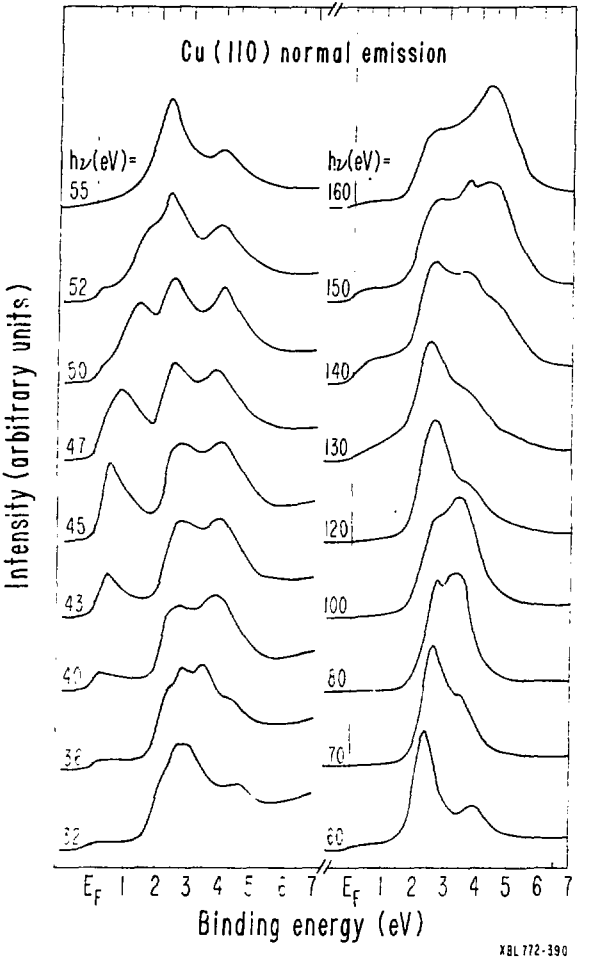
Cu (110) normal emission
hν(eV)=
55
52
50
47
45
43
40
38
32
hν(eV)=
160
150
140
130
120
100
80
70
60
Intensity (arbitrary units)
E_F 1 2 3 4 5 6 7
E_F 1 2 3 4 5 6 7
Binding energy (eV)
XBL 772-390

Figure 4

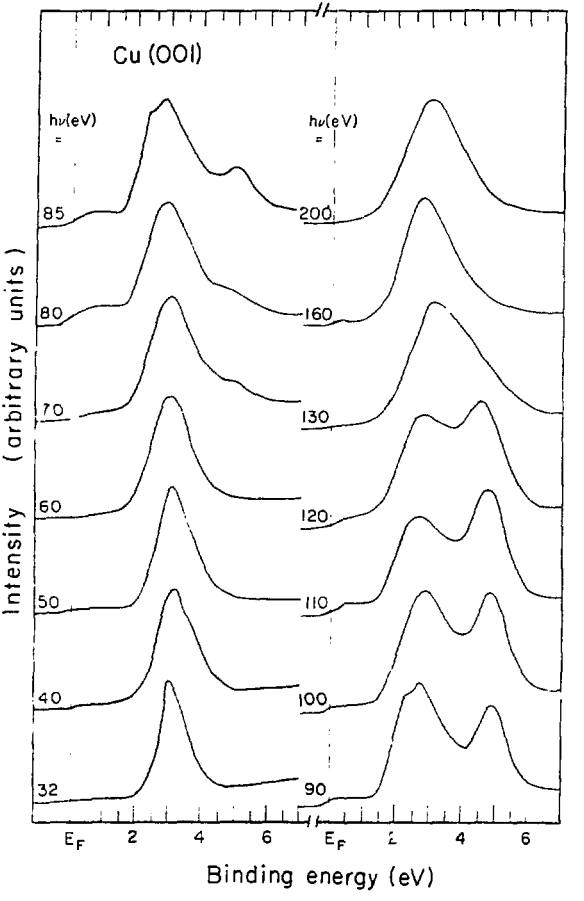

XBL 784-7994

Figure 5

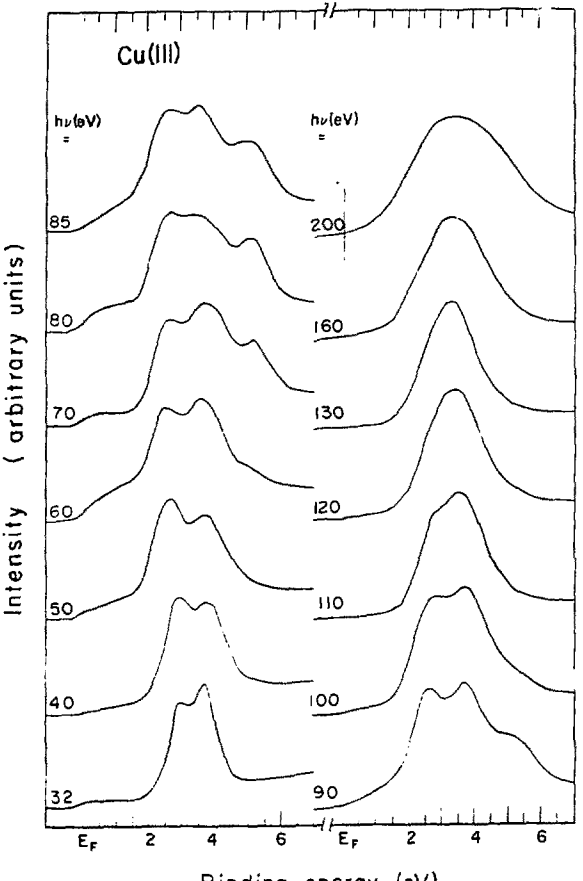

Figure 6

XBL 784-8025

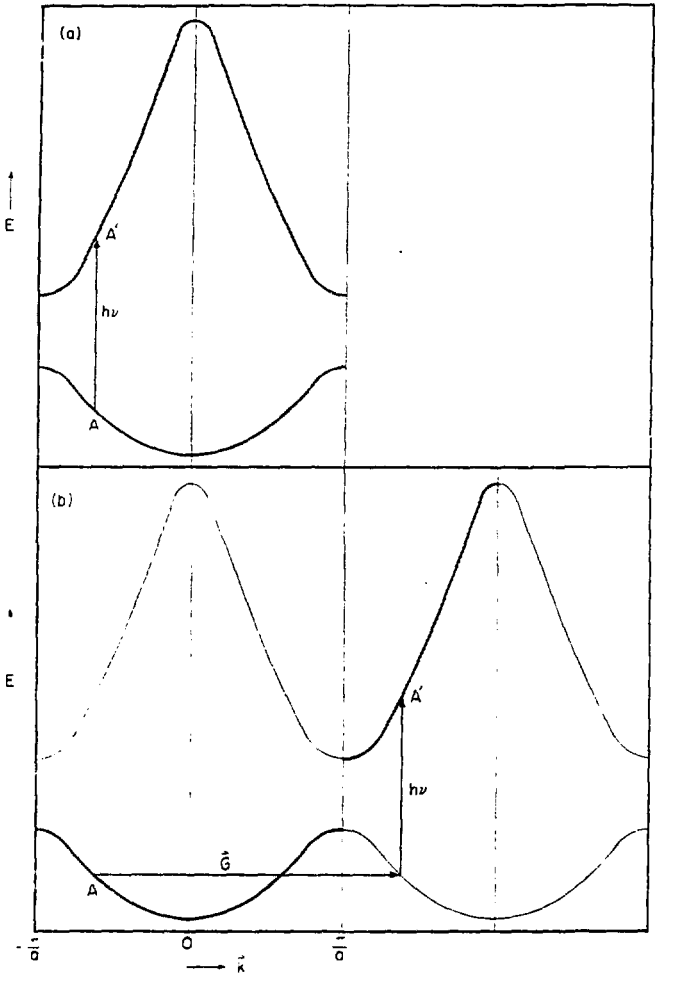

XBL 784-7995

Figure

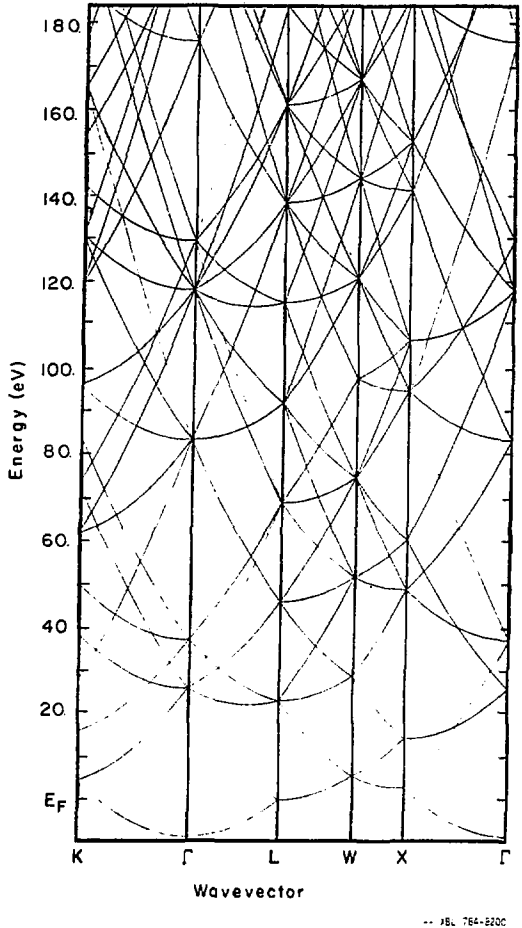
180.
160.
140.
120.
100.
80.
60.
40
20.
E_F
Energy (eV)
K
Γ
L
W
X
Γ
Wavevector
-- XBL 764-2200

Figure 3

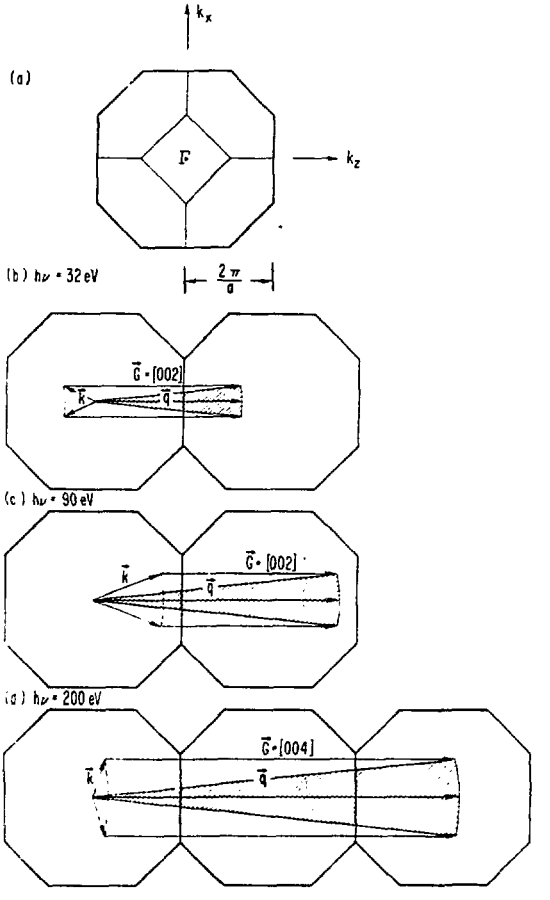

XBL 7611-4376

Figure 9

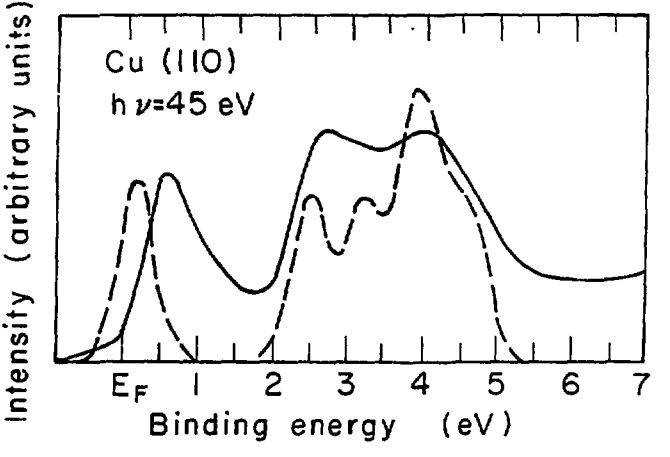
Cu (110)
h ν=45 eV
Intensity (arbitrary units)
E_F
1
2
3
4
5
6
7
Binding energy (eV)
XBL 777-1374

Figure 10

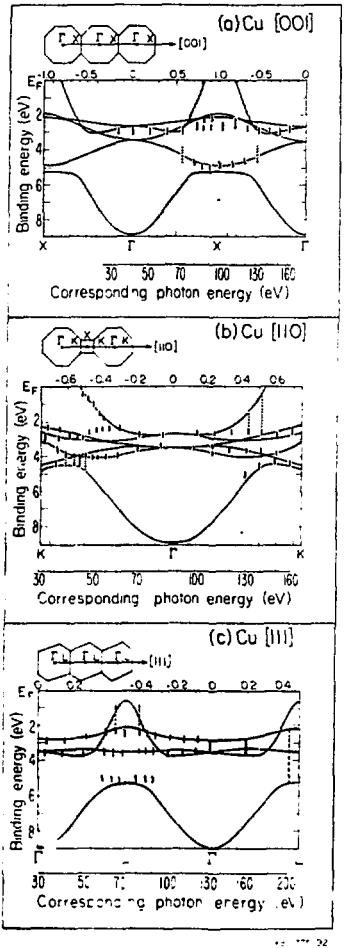
(a) Cu [001]
[001]
Binding energy (eV)
X
Γ
X
Γ
Corresponding photon energy (eV)
(b) Cu [110]
[110]
Binding energy (eV)
K
Γ
K
Corresponding photon energy (eV)
(c) Cu [111]
[111]
Binding energy (eV)
Corresponding photon energy (eV)

Figure 11

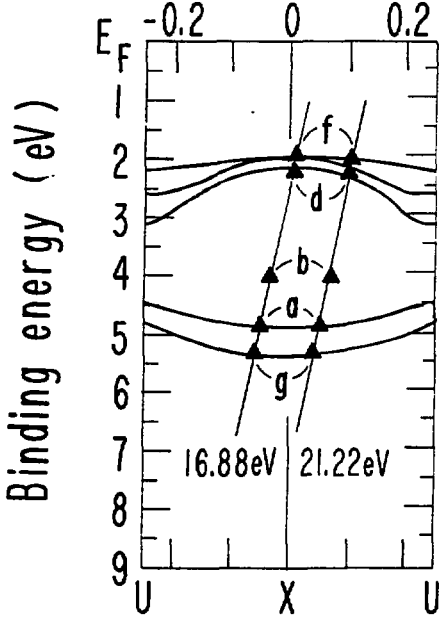

XBL 784-7988

Figure 12

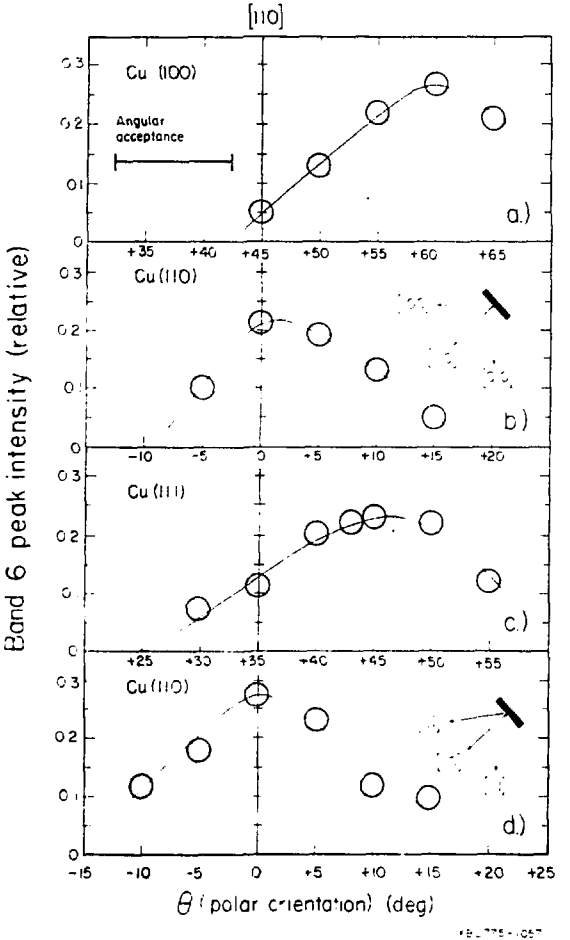
[110]
Cu (100)
Angular acceptance
a.)
Cu (110)
b)
Cu (111)
c.)
Cu (110)
d.)
Band 6 peak intensity (relative)
θ (polar orientation) (deg)

Figure 13

IV. BREAKDOWN OF THE DIRECT TRANSITION MODEL

A. Introduction

In the preceding chapter of this thesis it was demonstrated how a very simple model of photoemission, the Direct Transition (DT) model, can be used to interpret angle-resolved photoemission (ARP) spectra. Indeed, using this model and energy-dependent angle-resolved normal photoemission the bulk band structure of copper was mapped out along three different directions in the Brillouin Zone (BZ); Γ to K, Γ to L, and Γ to X (see Fig. 11 in Chapter III). Unfortunately, as with any other simple model, there are severe problems with this description of photoemission, and the applicability of the model depends critically on a careful choice of experimental parameters. In particular, we shall in this chapter identify and discuss three effects which have a significant influence on the resolution in $\vec{k}$-space and, therefore, a severe impact on the DT model.

The first effect we shall consider is that resulting from the finite mean-free-path of an electron in a solid (for typical values of the mean-free-path for electrons in solids see Fig. 9 and Ref. 14 in Chapter II). Shortening of the mean-free-path results in an uncertainty or "broadening" in the value of the component of $\vec{k}$ perpendicular to the surface of the sample (1); while even in the most surface sensitive regions this does not lead to a complete breakdown in the DT model, it nevertheless implies a lessening in the $\vec{k}$-resolution obtainable. In Sections IV.C and IV.D we will discuss two additional effects, thermal disorder and band-mixing, both of which lead to a complete breakdown of the DT model; thermal disorder will be shown to cause a breakdown in the

DT model at temperatures high in comparison to the sample Debye temperature, and band-mixing will be shown to result in a breakdown of the DT mode at high photon energies, i.e., Al Kα (1486.6 eV).

B. Momentum Broadening

In contrast to the situation that prevails in ultraviolet photoemission ($h\nu < 40$ eV), where the mean-free-path (λ_e) of an electron in a solid is typically on the order of tens of angstroms (see Fig. 12 in Chapter II), the photoelectron mean-free-path in the electron kinetic energy region around 100 eV is quite short. For electron energies near 100 eV, λ_e becomes comparable with the interatomic distance between layers in a solid (see Fig. 12 in Chapter II), and as a result the elastic photocurrent emanating from a sample in this energy range arises largely from the outermost 1-3 atomic layers of the sample. As discussed by Liebelman and Eastman (I) and more recently by Feuerbacher and Willis (I) such inelastic damping, which restricts the source region of the photocurrent near the surface, results in an uncertainty or "broadening" in the component of the final-state momentum normal to the surface ($k_\perp$). To estimate the magnitude of the uncertainty in $k_\perp$ for the case of copper and the photon energies employed in the studies reported in Chapter III, the uncertainty principle ($\Delta k \Delta x \geq \frac{1}{2}$) has been invoked; the values for Δx were those determined for the mean free-path of an electron in copper as a function of the kinetic energy of the electron (see Fig. 1). The maximum amount of smearing (broadening) calculated in this fashion corresponds to only *ca.* 10% of the width of the first BZ, and therefore does not lead to a complete breakdown of the

DT model; however, this amount of broadening can have a significant effect on the photoemission spectrum. To illustrate this, let us consider photoemission in the [110] direction from copper.

Fig. 2a shows the band structure for copper along the Γ to K direction (3) in the extended zone scheme. Superimposed on the valence band structure are the nominally free-electron final-state bands (shifted down by the appropriate photon energy) that are sampled at 45 and 140 eV photon energy, respectively. Assuming no broadening in the final-state momentum and the DT model described in Chapter III, one would expect to observe a peak in the photoemission spectrum wherever the final-state band intersects an initial state band, i e , one would expect peaks at ∿0.7 eV, ∿2.8 eV, ∿4.0 eV, and ∿4.7 eV binding energy in the photoemission spectrum at both 45 eV and 140 eV photon energy. Inspection of the spectra obtained at these photon energies, which are shown in Fig. 3, shows that for the hν = 45 eV spectrum the expected structure is indeed observed, though the peak at ∿4.7 eV binding energy is rather weak and not clearly resolved. At hν = 140 eV, the expected structure for binding energy greater than 2.0 eV is again observed; however, the intense peak in the s - p band observed at hν = 45 eV is not present.

The reason for the absence of this feature in the spectrum at hν = 140 eV is readily understood when momentum broadening in the final state is considered. Due to the finite path length of the final state, where initially a discrete set of allowed final states existed, there is now a semi-continuum of available final states into which an electron can be excited; this is shown in Fig. 2b (4). As seen in Fig. 2b, the

broadening is fairly small for electron energies near 45 eV (only ca. 5% of $\frac{2\pi}{a}$, where a is the lattice constant of copper) and therefore does not have a large effect on the features in the photoemission spectrum; however, for electron energies in the range 130-140 eV the broadening amounts to almost 10% of the width of the BZ, which is sufficient to smear out any sharp peak in the s - p band due to the steepness of the band giving rise to this feature. Indeed, momentum broadening in the final state poses a serious problem in the use of photon energy dependent ARP studies to map out the details of the bulk band structure of materials, and is an effect which must be considered when such studies are carried out.

C. Thermal Disorder

The temperature and energy dependence of the intensity of elastically scattered radiation (e.g., x-rays, neutrons, or electrons) by a crystal lattice is governed by the Debye-Waller factor

$$f = \exp -(\langle \vec{q}\cdot\Delta\vec{r})^2\rangle \ . \qquad (1)$$

Here $\vec{q} = \vec{k}_f - \vec{k}_i$ is the difference between the incident (initial) and scattered (final) wavevector of the radiation and $\Delta\vec{r}$ is the instantaneous thermal displacement of an atom from its equilibrium lattice position. Angle-resolved photoemission may also be viewed as a scattering process: in a simple one-electron picture the initial state involves a photon with wavevector $\vec{k}_{ph}$ and a bound (e.g., valence) electron with wavevector $\vec{k}_e$ ($\vec{k}_i = \vec{k}_{ph} + \vec{k}_e$), while the final state is characterized by the photoelectron with wavevector $\vec{k}_f$. The diffraction law $\vec{k}_f - \vec{k}_i =$

', where $\vec{G}$ is a reciprocal lattice vector, describing the elastic scattering of radiation by a crystal lattice, also describes the direct transition requirement in ARP (see Chapter III). It follows therefore that the intensity of a direct-transition peak in ARP should exhibit a temperature and energy dependence governed by f. Furthermore, the indirect (phonon-assisted) transition channel in photoemission can be shown to correspond closely to the thermal diffuse scattering process in x-ray diffraction (5); this correspondence between x-ray diffraction and ARP is manifested in the photoexcitation matrix element (6,7)

$$\langle f|\vec{A}\cdot\vec{p}\,e^{i\vec{q}\cdot\vec{r}}|i\rangle^2 \propto |c_1(\vec{k}_f)|^2(1-f) + |c_1(\vec{k}_f-\vec{k}_i-\vec{G})|^2 f \quad . \qquad (2)$$

Eq. (2) was derived assuming an LCAO tight-binding initial state and plane-wave final state wavefunctions. Here, $c_1(\vec{k}_f)$ is an atomic type matrix element. The importance of the direct (i.e., $\vec{q} = \vec{G}$) relative to the indirect transition term in Eq. (2) depends on both temperature and photon energy. Although the photon energy does not enter explicitly in Eq. (2), it is contained in $\vec{q}$ since with increasing photon energy the photoelectron wavevector (and hence $\vec{q}$) increases.

To illustrate the influence of temperature on ARP spectra let us consider angle-resolved normal photoemission from a Cu(110) single crystal for $h\nu$ = 45 eV. At room temperature the spectrum obtained from a Cu(110) at $h\nu$ = 45 eV is dominated by direct transitions as discussed in Chapter III and Section B above (see Figs. 2a and 3). The spectrum is characterized by the presence of a very pronounced peak in the s - p band portion of the spectrum at ca. 0.5 eV binding energy (see Fig. 3), which is an extremely sensitive indicator of the direct transition

channel because it originates only from transitions in a very small region of the BZ. As the temperature of the sample is raised incrementally to 870°C (see Fig. 4) the intensity of this peak decreases monotonically (Fig. 5). In Fig. 5, the temperature dependence of this peak is compared with that of the Debye-Waller factor f_n (n = 1,2,3), where the index n denotes different calculations assuming a mean square displacement of n times the bulk value; the bulk value of $\langle r_x^2 \rangle$ were taken from temperature diffuse scattering data [9]. Because mean square displacements normal to the surface are larger for the surface layer than for the bulk [1], photoemission, due to its more surface sensitivity, is expected to agree most with n = 4, as is observed. The faster decrease in the intensity of the peak in the 4 - 5 eV band between 800°C and 850°C compared to f results from a temperature dependence of the ratio of $\langle r_x^2 \rangle_{surface}$ to $\langle r_x^2 \rangle_{bulk}$; the latter quantity increases with increasing temperature [11].

Changes in the d- band portion of the spectrum as a function of temperature are evident as well in Fig. 4. At high temperatures the d-band becomes asymmetric, with more intensity at the top of the bands, until at 870°C, the spectrum resembles that of polycrystalline copper for hν = 50 eV [12] (compare Figs. 4 and 6]. For copper, a single electron-phonon interaction can change the electron wavevector from the Γ point to anywhere within the BZ with no more than a 30 meV [13] change in the electron energy, thus allowing more of the $\vec{k}$ states in the BZ to be sampled without greatly disrupting their energy distribution.

It follows therefore that the direct-transition model describes

[illegible] ultraviolet energies only if the temperature is low [illegible] suppress phonon-assisted indirect transitions. Thermal meansquare displacements of atoms in crystals approach their limiting zero-point values for temperatures somewhat below the Debye temperature of the material in question. Thus, a general rule for obtaining a maximum amount of thermal momentum broadening is to collect ARP spectra at temperatures well below the surface Debye temperature.

[illegible]

[illegible] thermal disorder is taken into account, the measured photoemission cross-section is given as the sum of a k-conserving direct-transition term and an atomic scattering contribution from the two terms to the photoemission intensity is modified by the Debye-Waller factor (see Eq. (2) in Section [illegible]). For high temperatures and room temperature, f is less than [illegible] small, therefore, the phonon-assisted channel [illegible]. Hence, at x-ray energies and room temperature, [illegible] in the angle-resolved photoemission spectrum of a [illegible] would reflect anisotropies in the atomic cross-section [illegible], therefore, provide information concerning the orbital com[illegible] of the initial states; we shall discuss this point more fully [illegible]. In this section, we will be concerned with another effect, the temperature dependence of the angle-resolved x-ray photoemission [illegible] spectrum, which is equally interesting and which provides information on the nature of the final states sampled at x-ray energies.

Spectra were recorded for electrons propagating along the [100] direction of the [111] crystals and along the [111] direction of the [110] crystal [4].

The experimental results obtained from the two gold crystals are shown in Figs. 7 and 8. In each case the lowest (solid) curve is the experimental room-temperature result, and the middle (dashed) curve is the experimental spectrum observed at low-temperature (T ~95°K, see Ref.

[illegible] the direct transition model.

[illegible] that no changes are observed in [illegible] the experimental low- [illegible] and 8 are identical, within the [illegible], with the room-temperature results, and [illegible] agreement with the predicted curves.

[illegible], the experimental results in Fig. 9 lead to [illegible] conclusion, although several experimental parameters [illegible] different from the gold case. In particular, the Debye-Waller [illegible] larger for Pt than for Au at both room and lower temperatures. In addition, because the lattice constant is different, according to the direct transition model a different part of the BZ would be sampled

[illegible]

[illegible] experiments are needed to test the above proposal, it [illegible] is that we [illegible] a fractional restoration of direct-transition processes will be found at x-ray energies. There [illegible] between angle-resolved ultraviolet photoemission and XRPS, however, in which direct transitions are restored as ℓ is increased; correlation of the energy range and the form of this transition with the complexity of the final state would help answer one of the remaining questions about high-energy photoemission from crystalline solids.

[illegible]

[illegible] and I. I. Rabi, Phys. Rev. 81, 4 (1951).

[illegible] and I. I. Rabi, Phys. Rev. 81, 4 (1951).

[illegible] R. [illegible], "Electron Spectroscopy," p. 5, 4 (1974).

[illegible], "Electron Spectroscopy," p. [illegible].

[illegible], [illegible], 13 (1967).

[illegible] the total [illegible] was [illegible] using the [illegible] of [illegible] electron [illegible] [illegible].

[illegible], [illegible] Corporation (Cleveland, Ohio), p. 179-[illegible] (1969).

[illegible], private communication.

[illegible], J. [illegible], [illegible], and P. A. Shirley, Phys. [illegible], 5, 2 (1972). For a more general form of Eq. (2) see [illegible], [illegible] Ph.D. thesis.

[illegible] were carried out, with two different [illegible] and [illegible]. The spectral variations with temperature were reversible and reproducible. Magnetic fields induced [illegible] after the leads were calculated to deflect electrons by [illegible].

[illegible], International Tables for X-Ray Crystallography, C. H. MacGillavry, [illegible], and K. Lonsdale, eds. The Kynoch Press, Birmingham, [illegible], 1962), p. 257.

[illegible], P.C. Clark, and R. Herman, Phys. Rev. 167, 652 (1968).

[illegible] R. Hasel, private communication.

[illegible]

[illegible]

[illegible]

[illegible]

[illegible]

FIGURE CAPTIONS

Fig. 1: [illegible] electron mean-free-path in copper as a function of the electron kinetic energy [2]. The region between [illegible] and [illegible] is shown as a dashed line because no experimental or theoretical results are available in this region.

Fig. 2: [illegible] band structure of copper [3] along the [illegible] direction [illegible] are [illegible] normally free-electron final-state band [illegible] shifted [illegible] the appropriate [illegible] that are sampled at 45 and 140 eV photon energy, [illegible] direct transitions [illegible] where the final-state band intersects an initial state band.

Fig. 3: [illegible] momentum broadening in the final state has been included [4]. All final states in the cross-hatched region are now allowed.

Fig. 4: [illegible] photoemission spectra obtained from the valence band of a Cu(110) single crystal at hν = 45 eV and 140 eV. The spectra were collected normal to the (110) face with an angular resolution of ±5°.

Fig. 5: Temperature dependence of the angle-resolved normal photoemission spectrum from a Cu(110) crystal at hν = 45 eV. The angular resolution was ±5° and the energy resolution was ≤ 0.2 eV.

Fig. 5 Experimental intensity of the peak at 7.1 eV binding energy in Fig. 4 as a function of temperature (full circles connected by a solid line) compared to the Debye-Waller factor e^{-2M} (solid line). The different curves for e^{-2M} correspond to calculations with $\bar{u}$, the mean-square displacement of a lattice atom, equal to the bulk value, $\bar{u}$, and $2\bar{u}$.

Fig. 6 Valence band photoemission spectrum of polycrystalline copper at 300°K. Experimental resolution was 0.30 eV.

Fig. 7 Valence band photoemission spectra for Ni valence band electrons along the [111] crystalline direction. The lowest (full circles) are the experimental spectra at room temperature. The middle curve is the experimental spectrum at liquid nitrogen temperature. The top curve is the expected spectrum at liquid nitrogen temperature, based on the direct transition model. The curves are offset for clarity.

Fig. 8 Valence band x-ray photoemission spectra for Au valence band electrons along the [100] direction. The format is the same as in Fig. 7.

Fig. 9 Valence band x-ray photoemission spectra for Pt valence band electrons along the [100] direction. The format is the same as in Fig. 7.

Fig. 10 High energy bands of Cu in the free-electron approximation, along symmetry directions.

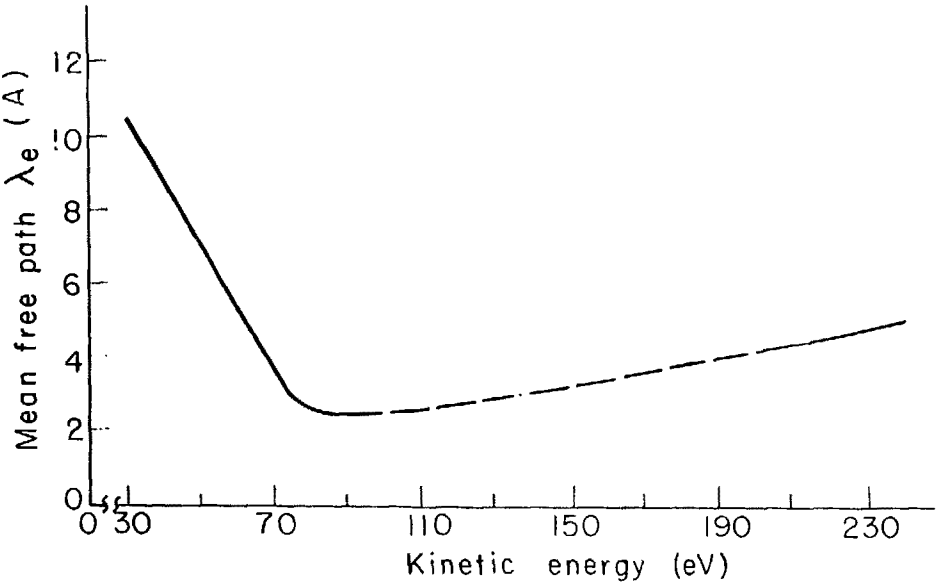

XBL 777-1375

Figure 1

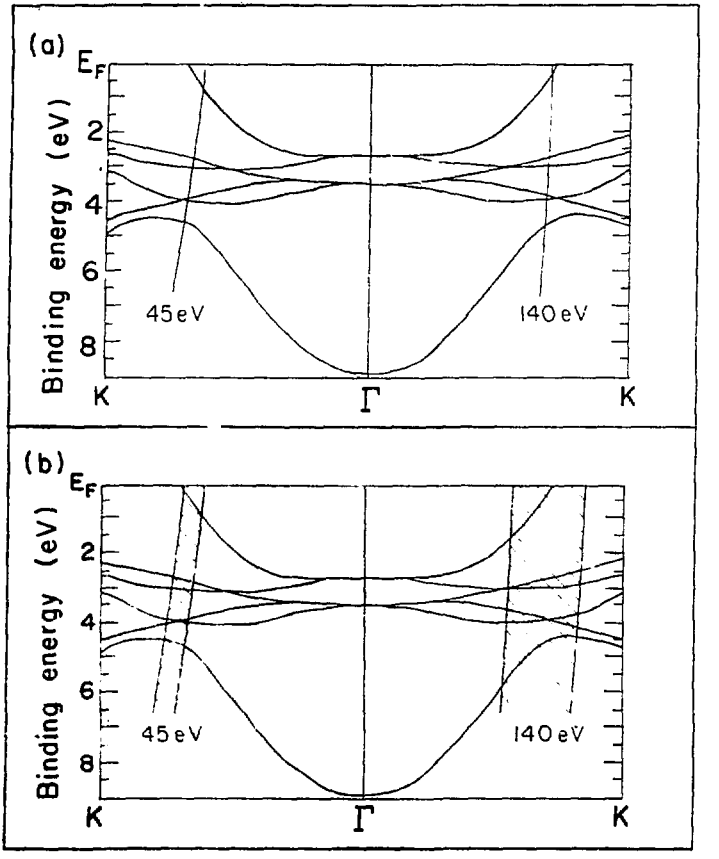

XBL 784-7993

Figure 2

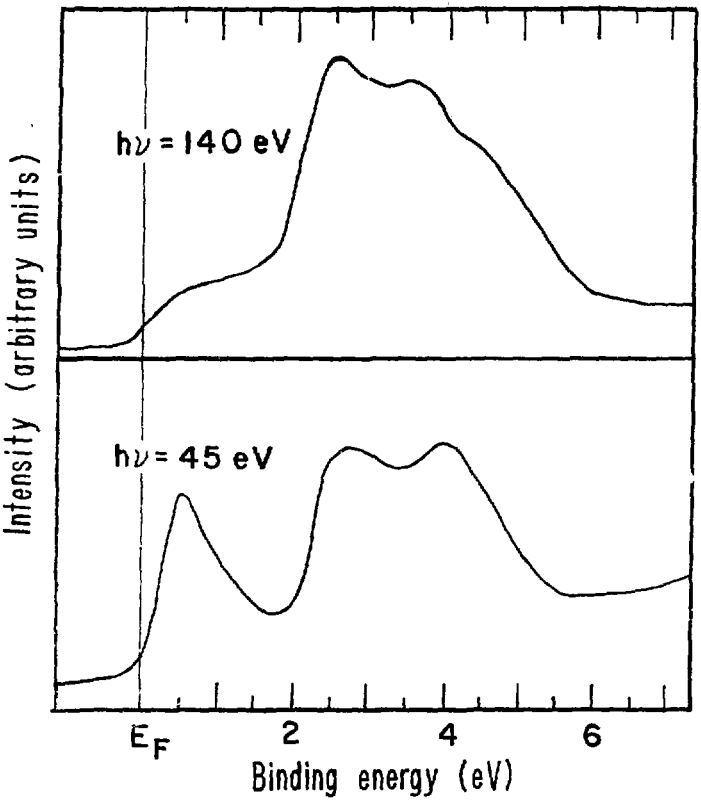

Figure 5

XBL 784-7969

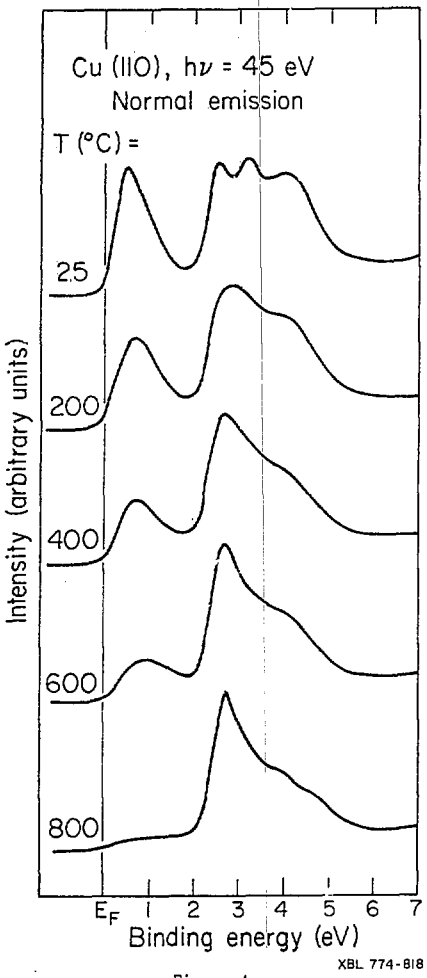
Cu (110), hν = 45 eV
Normal emission
T (°C) =
25
200
400
600
800
Intensity (arbitrary units)
E_F
1
2
3
4
5
6
7
Binding energy (eV)
XBL 774-818

Figure 4

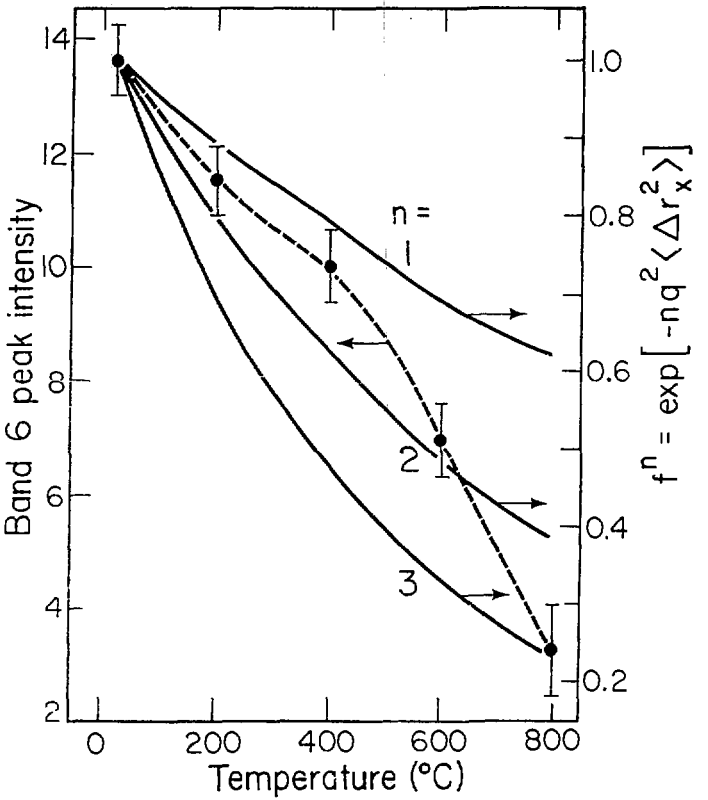

XBL 784-7991

Figure 5

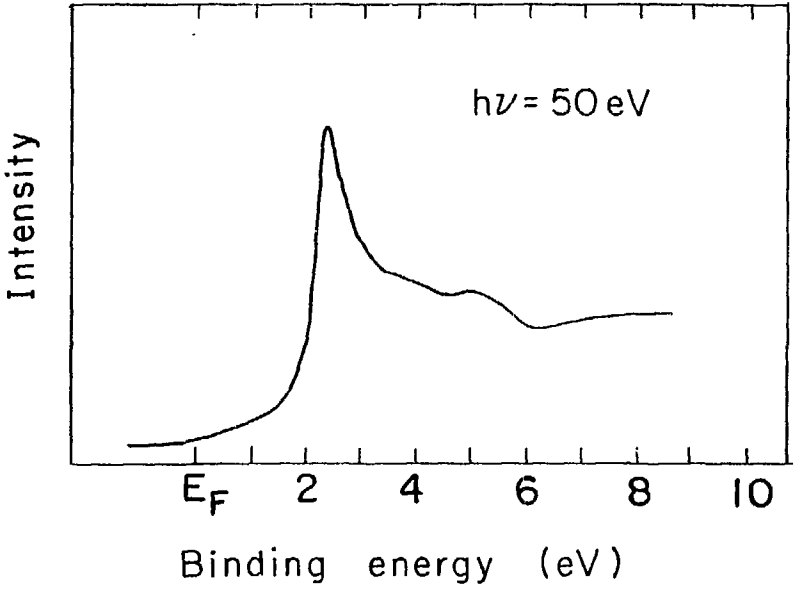

Figure 6

XBL 784-7987

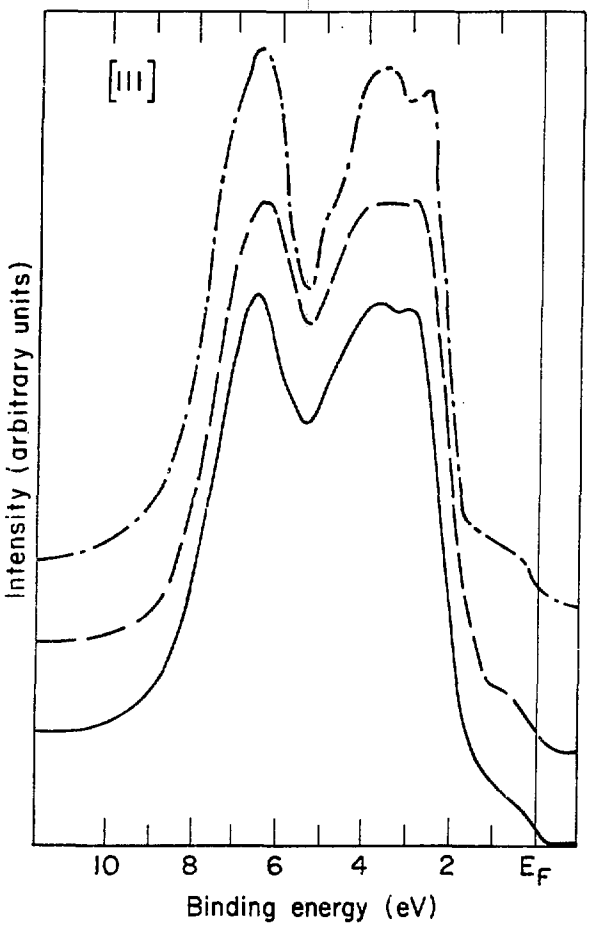
[111]
Intensity (arbitrary units)
10
8
6
4
2
E_F
Binding energy (eV)
XBL 7710-2021

Figure 7

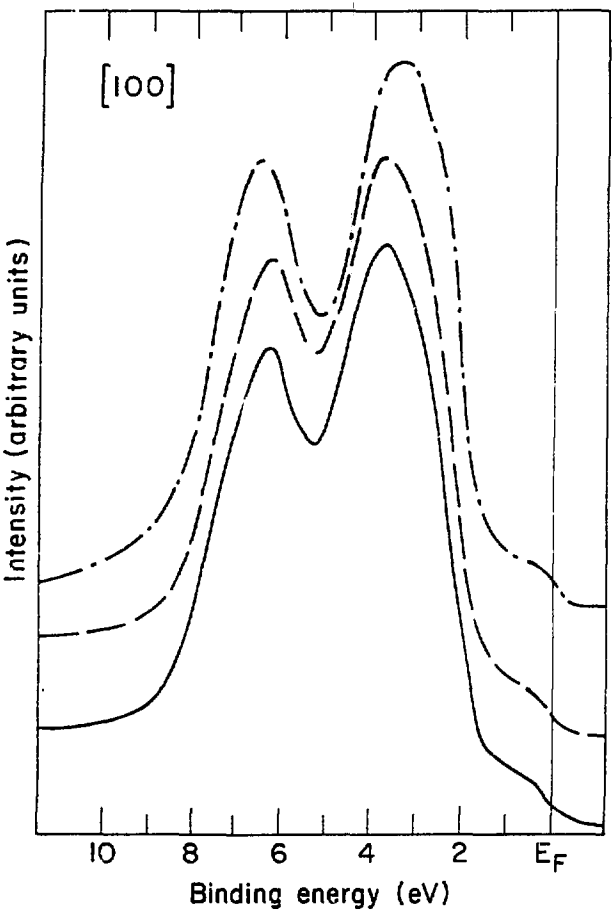

XBL 7710-2020

Figure 8

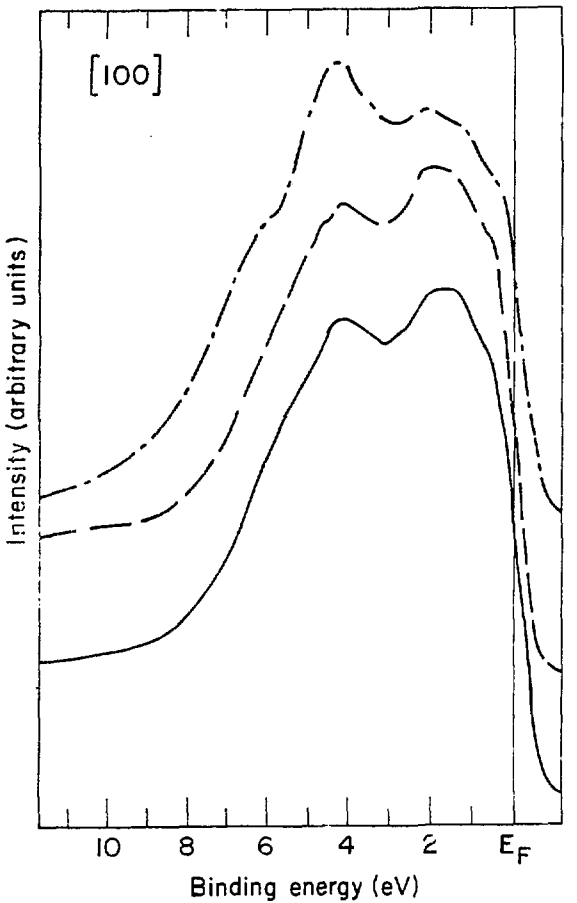
[100]
Intensity (arbitrary units)
10
8
6
4
2
E_F
Binding energy (eV)
XBL7710-2019

Figure 9

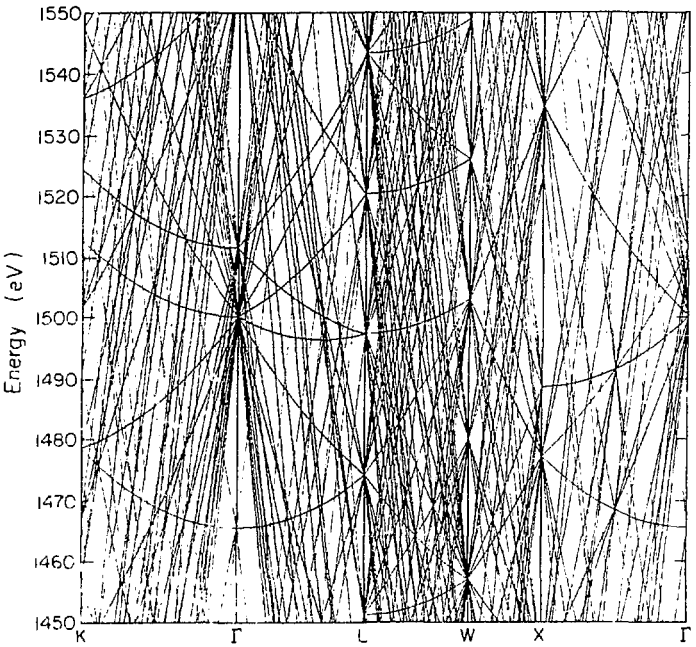
1550
1540
1530
1520
1510
1500
1490
1480
1470
1460
1450
Energy (eV)
K
Γ
L
W
X
Γ
XBL77.2-11079

Figure 10

V. ANGLE-RESOLVED X-RAY PHOTOEMISSION FROM SINGLE CRYSTALS

A. Introduction

The Direct Transition theory of photoemission developed in Chapter III of this thesis has had considerable success in explaining variations in angle-resolved ultraviolet photoemission data ($h\nu \leq 250$ eV) obtained from single crystals, both as a function of the electron emission angle (1) and of the incident photon energy (2), in terms of sampling different portions of the first Brillouin Zone (BZ). As discussed in the preceding chapter, however, thermal disorder and the complexity of the final-state at high energies lead to the expectation that the model will not describe angle-resolved x-ray ($h\nu \geq 1000$ eV) photoemission (ARXPS) data. Indeed at such energies the requirements of momentum and energy conservation should be easily satisfied throughout the first BZ, and variations with angle in the ARXPS spectrum of a single crystal should reflect anisotropies in the atomic cross-section and should, therefore, provide valuable information concerning the orbital composition of the initial states. In this chapter, an elementary model will be presented. Based on a single plane wave final state and a tight-binding initial state, it allows for the interpretation of ARXPS spectra in terms of the symmetry properties of the initial state wavefunctions. In addition, calculations using this model will be shown to be in excellent agreement with experimental results for ARXPS from the valence bands of copper single crystals.

B. Experimental Details and Results

Two single crystals of copper with (001) and (111) surface

orientation, respectively, were prepared as described in Section C of Chapter II of this thesis. The crystals were then mounted in a Hewlett-Packard 5950A ESCA spectrometer where they were further cleaned by argon ion bombardment and annealed by heating with an electron gun to remove surface damage caused by the bombardment. Cleanliness of the surfaces was checked by monitoring the carbon and oxygen 1s core lines, both of which were undetectable during the course of the measurements. Spectra were recorded for electrons propagating along the [001] direction of the (111) crystal and along the [111] direction of the (001) crystal; the detailed experimental geometry is summarized in Fig. 1. In both cases the nominal electron take-off angle, measured from the sample surface, was 35.5°. The experimental angular resolution was ±4°, while the energy resolution was constant at 0.8 eV.

Spectra acquired from the valence band region of copper using Al Kα radiation ($h\nu = 1486.6$ eV) are shown in Fig. 2a. The first spectrum was obtained previously from an evaporated polycrystalline copper film, while the other two spectra were recorded using the single crystal samples. It should be mentioned that all the spectra shown in Fig. 2a represent raw data, without any smoothing, deconvolution, or background subtraction. In Fig. 2b the detailed shapes of the Cu[111] and Cu[001] spectra are compared; it is apparent that a distinct change in the spectral shape exists between the two angle-resolved photoemission spectra.

C. Matrix-Element Model

Within the one-electron model of photoemission, the photoelectron

energy distribution (PED) is given by the following expression (3):

$$N(E, h\nu) \propto \int_{BZ} d^3k \sum_{j,f} |t_{fj}(\vec{k})|^2 \delta(\vec{k}_f - \vec{k} - \vec{k}_{h\nu} - \vec{G}) X$$

$$\delta[E_f(\vec{k}) - E_j(\vec{k}) - h\nu] \delta[E(\vec{k}) - E_j(\vec{k})] \quad . \qquad (1)$$

Here $t_{fj}(\vec{k})$ is a transition matrix element between an initial state of wavevector $\vec{k}$ and energy $E_j(\vec{k})$ and a final state of wavevector $\vec{k}_f$ and energy $E_f(\vec{k})$. The two Kronecker delta functions represent the requirements of wavevector (momentum) and energy conservation in the excitation process, with that for momentum resulting from a sum over lattice sites. $\vec{k}_{h\nu}$ is the wavevector of the incident radiation, and $\vec{G}$ is a reciprocal lattice vector.

As discussed in Chapter III of this thesis, at ultraviolet energies (i.e., $h\nu \leq 250$ eV), the delta function corresponding to momentum conservation and to a lesser extent that representing energy conservation are responsible for most of the variations observed in angle-resolved photoemission spectra both as a function of the propagation direction of the electron and the energy of the incident photon beam; the matrix-element for most purposes may be assumed to be constant. At x-ray energies ($h\nu \geq 1000$ eV), however, the situation is quite different, as was briefly discussed in Sections IVC and IVD. The delta function representing momentum conservation is relatively easily satisfied for states throughout the first BZ for any arbitrary angle of emission at x-ray energies, due to the complexity of the final-state sampled at high energies (see Fig. 10 in Chapter IV) and the finite angular resolution of the measurements. (Another reason for the lack of a

strong dependence on the selection rule for momentum at x-ray energies, and perhaps equally important, was discussed in Section IVC, namely, thermal disorder.) In addition, as discussed by McFeely and co-workers (4), due to the large number of final states available at x-ray energies (see Fig. 10 in Chapter IV) and the mixing of these states by the crystal potential (5), the delta function in Eq. (1) representing energy conservation in the excitation process should also be easily fulfilled for states throughout the BZ for any arbitrary angle of electron emission at high energies. Hence, in contrast to the situation at u.v. energies where the delta functions play such a dominant role and serve to restrict the portion of the BZ which can contribute to an angle-resolved photoemission spectrum (see Chapter III), at x-ray energies the delta functions are rather unimportant; that is, they are easily satisfied, and states throughout the entire BZ contribute to an ARXPS spectrum.

With the above result, angle-dependent PED's observed at x-ray energies are given by the initial density of states where the various bands at each $\vec{k}$-point within the first BZ are weighted by an angle-dependent transition matrix-element (4). As was shown in Ref. 4, this transition matrix element may conveniently be calculated by writing the initial state wavefunction in the tight-binding form (6) and assuming a plane-wave final state. Neglecting the s-part of the initial state wavefunctions, which only contributes a small and isotropic matrix element, the following angle-dependent matrix element is obtained:

$$\sigma(\vec{k},j,\vec{q}) \sim \left| \sum_{\mu=1}^{5} \beta_{\mu}^{j}(k)\ d_{\mu}(\theta_q,\phi_q) \right|^2 \quad . \tag{2}$$

Thus, the intensity distribution of photoemitted electrons may be discussed in terms of the Fourier transformed d-orbitals $d_{\mu}(\theta_q,\phi_q)$ listed in Table I. Here $\vec{q}$ is the wavevector of the photoexcited electron inside the crystal and the coefficients $\beta_{\mu}^{j}(\vec{k})$ are obtained from a band-structure calculation (6-8). Because the whole BZ is sampled, Eq. (2) may be further simplified by grouping the matrix elements of all equivalent points in the first BZ. The matrix elements of all equivalent points are obtained by transforming the d-orbitals under the respective point-group operations (9). In this way it is seen that the various cross-terms which occur in Eq. (2) cancel and one obtains the following analytical expression for the matrix element (compare Appendix A)

$$\sigma(\vec{k},j,\vec{q}) \sim 2\left(|\beta_1^j|^2 + |\beta_2^j|^2 + |\beta_3^j|^2\right)\left(d_1^2 + d_2^2 + d_3^2\right) + 3\left(|\beta_4^j|^2 + |\beta_5^j|^2\right)\left(d_4^2 + d_5^2\right) \quad . \tag{3}$$

Equation (3) demonstrates that the angle dependent matrix element is in general a linear combination of the t_{2g} and e_g projections of the initial state tight-binding function:

$$\sigma_{t_{2g}}(\vec{k},j) \sim |\beta_1^j|^2 + |\beta_2^j|^2 + |\beta_3^j|^2 \tag{4}$$

and

$$\sigma_{e_g}(\vec{k},j) \sim |\beta_4^j|^2 + |\beta_5^j|^2 \quad . \tag{5}$$

Because in the derivation of Eq. (3) the wavefunctions at all equivalent points in the first BZ were transformed into one irreducible wedge of the BZ, Eq. (3) may be used as a weighting factor for a density of states calculation in 1/48 of the BZ. The angle-resolved photoemission spectrum in the XPS limit is then given by the following expression

$$N(E,\vec{q}) \sim \int_{\substack{1/48 \\ BZ}} d^3k \sum_j \sigma(\vec{k},j,\vec{q})\ \delta(E - E_j(\vec{k})) \quad . \tag{6}$$

It should be noted that according to Eq. (3), photoemission along the [001] direction (i.e., $\theta_q = \phi_q = 0°$ and therefore $d_1 = d_2 = d_3 = 0$) and along the [111] direction (i.e., $\theta_q = 54.7°$, $\phi_q = 45°$ and therefore $d_4 = d_5 = 0$) represent the two extreme cases corresponding to the e_g and t_{2g} projections of the density of states (10), respectively.

At this point a comment on previous calculations of the XPS photoemission spectra of polycrystalline d-band materials by Nemoshkalenko and co-workers (11) is in order. These authors claimed that by including angle averaged (integrated) matrix elements between tight binding d-initial states and plane wave final states, they could account for part of the discrepancy between the experimental spectra and the calculated density of states. In particular they concluded that the electron excitation probability from e_g states is higher than from t_{2g} states. The calculations reported here, which employed the same description of initial and final states, is in disagreement with their result, since for polycrystalline materials, i.e.,

angle-integrated matrix elements, the e_g and t_{2g} states contribute equally to the photoemission spectrum. Equations (1) and (2) show that for this case the cross section (which is proportional to the transition probability) is given by

$$\sigma(k,j,q) \sim \sum_m |g_m^j(\vec{k})|^2 \quad . \tag{7}$$

This is exactly the *total* d-projection of the initial states, i.e., the sum of the e_g and t_{2g} projections (12). Only in the case of angle resolved photoemission from an oriented single crystal face can the cross sections for photoemission from e_g and t_{2g} states be different.

Finally, throughout the above discussion it has been assumed that the photoelectron angular distribution is the same inside and outside the crystal, i.e., refraction of the photoelectron at the crystal-vacuum interface has been neglected. This may be justified by noting that if the final Bloch state contains the reciprocal lattice vector $\vec{G}$, a photoelectron with wavevector $\vec{k}_{h\nu} + \vec{k} + \vec{G} = \vec{q}$ is produced inside the crystal. The electron is then transmitted through the surface into a direction $\vec{p}$ outside the crystal, where $|\vec{p}|$ is related to the kinetic energy E_{kin} of the photoelectron according to

$$E_{kin} = \hbar^2 |\vec{p}|^2/2m \quad . \tag{8}$$

If α is the angle of incidence between $\vec{q}$ and the surface normal and β is the angle of refraction between $\vec{p}$ and the crystal normal, the boundary conditions are $\vec{p}_{\parallel} = \vec{q}_{\parallel}$ and $\sin\beta/\sin\alpha = |\vec{q}|/|\vec{p}|$ (23). The ratio $|\vec{q}|/|\vec{p}|$ which at XPS energies is essentially unity for free

electron final states may deviate from 1 for Bloch-type final states because states throughout the first BZ are sampled, causing $\vec{q}$ to deviate from the free electron value. Since at XPS energies $\vec{G} \gg \vec{k}$ the ratio $\vec{G}/\vec{p}$ is still approximately unity, however, and therefore, refraction at the solid-vacuum interface may be neglected, except at low take-off angles.

D. Discussion of Results

In Fig. 2c the results of a theoretical model calculation employing Eq. (1) for photoemission from the valence bands of copper single crystals into the [111] and [001] directions are shown. As discussed earlier these cases correspond to the t_{2g} and e_g projections of the valence band density of states. Comparison of Figs. 2b and 2c reveals good agreement between the experimental and theoretical PED's. The main characteristic differences between the experimental spectra taken along the two symmetry directions are predicted well by the calculation. It should be noted that plane wave final state cross section calculations should be more reliable for Cu than for the previously investigated noble metals Ag and Au (4); this is suggested by the smaller electron scattering phase shifts for Cu as opposed to Ag and Au (14). Also, the spin-orbit coupling which reduces the e_g-t_{2g} anistropy by mixing the wavefunctions is small for Cu; this might explain why the experimental and theoretical differences between the two directions are quite pronounced for Cu. It is interesting to note that the theoretical model predicts that the largest changes will occur between the PED's taken along the [001] and [111] directions; this is in

complete agreement with the experimental findings of Baird and co-workers for Au (15). More evidence for the importance of matrix element effects in x-ray photoemission from d-bands, as opposed to the constant matrix element model proposed by Baird *et al.* (15), was recently presented by Williams and co-workers (16). These authors found good agreement between the experimental angular variation of valence band peak intensities of MoS_2 and that predicted by a tight-binding d-initial and plane-wave final state matrix element model. The present results in conjunction with the results obtained previously for Ag and Au (4) indicate that the model presented above for explaining the angular dependence of photoemission from d-bands may *in general* provide a useful approximation in the x-ray range of photoemission.

APPENDIX A: TRANSFORMATION OF TIGHT BINDING d-FUNCTIONS IN A FIELD OF CUBIC SYMMETRY

Let $\psi^j_{\vec{k}}(\vec{r})$ be a tight binding Bloch function

$$\psi^j_{\vec{k}}(\vec{r}) = N^{-\frac{1}{2}} \sum_{\ell} e^{i\vec{k}\cdot\vec{R}_\ell} \chi_j(\vec{r} - \vec{R}_\ell) \tag{A1}$$

where $\chi_j(\vec{r} - \vec{R}_\ell)$ is a linear combination of atomic orbitals (LCAO)

$$\chi_j(\vec{r}) = \sum_{\mu} \beta^j_\mu(\vec{k})\ \phi_\mu(\vec{r}) \tag{A2}$$

Let P be an operator, corresponding to one of the operations of the cubic group, (9) i.e., an operator which transforms a point $\vec{k}$ from one irreducible zone of the first BZ into an equivalent point in a different irreducible zone. Then the transformation of the corresponding Bloch function under P is given by (9)

$$P\psi^j_{\vec{k}}(\vec{r}) = \psi^j_{\vec{k}}(P^{-1}\vec{r}) = N^{-\frac{1}{2}} \sum_{n} e^{i\vec{k}\cdot\vec{R}_n} \chi_j(P^{-1}\vec{r} - \vec{R}_n) \tag{A3}$$

where

$$\chi_j(P^{-1}\vec{r}) = \sum_{\mu} \beta^j_\mu(\vec{k})\ \phi_\mu(P^{-1}\vec{r}) \tag{A4}$$

Thus the transformation of the tight binding function $\psi^j_{\vec{k}}(\vec{r})$ is accomplished by simply transforming the atomic functions $\phi_\mu(\vec{r})$ under the inverse operation P^{-1}. Furthermore, $\phi_\mu(\vec{r})$ may be separated into a radial part R(r) and an angular part $d_\mu(\theta_r,\phi_r)$. In the case of a simple fcc lattice the operations of the cubic group only affect the angular part, i.e., the d-orbitals $d_\mu(\theta_r,\phi_r)$. Thus

$$\chi_j(P^{-1}\vec{r}) = R(r) \sum_\mu \beta_\mu^j(\vec{k})\ P^{-1} d_\mu(\theta_r, \phi_r) \ . \qquad (A5)$$

Knowing how the wave function $\psi_{\vec{k}}^j(\vec{r})$ transforms under P we can now transform its matrix element with a plane-wave given by Eq. (2). Since this matrix element is the Fourier transform of the function $\sum_\mu \beta_\mu^j(\vec{k})\ d_\mu(\theta_r, \phi_r)$, we obtain

$$\left| \sum_\mu \beta_\mu^j(\vec{k})\ P^{-1} d_\mu(\theta_q, \phi_q) \right|^2 \qquad (A6)$$

for the transformed matrix element. Hence it is only necessary to work out the transformations of the five d-orbitals under the 48 symmetry operations of the cubic group. This is easily done by writing the d-orbitals in cartesian coordinates. All t_{2g} orbitals (compare Table I) transform into each other (e.g., $P^{-1}d_2 = -d_3$) while the e_g orbitals either transform into themselves (i.e., $P^{-1}d_4 = d_4$ or $-d_4$ and $P^{-1}d_5 = d_5$) or into a linear combination of d_4 and d_5, i.e., $P^{-1}d_4 = -\frac{1}{2} d_4 \pm \sqrt{3}/2\ d_5$) and $P^{-1}d_5 = \pm \sqrt{3}/2\ d_4 - \frac{1}{2} d_5$. The sum of all 48 cross-sections given by Eq. (A6), corresponding to the 48 equivalent k points in the first BZ then yields Eq. (6).

REFERENCES

1. S.D. Kevan, P. S. Wehner, and D. A. Shirley, to be published.
2. D. A. Shirley, J. Stöhr, P. S. Wehner, R. S. Williams, and G. Apai, Physica Scripta XX, XXXX (1977); J. Stöhr, P. S. Wehner, R. S. Williams, G. Apai, and D. A. Shirley, Phys. Rev. B17, 587 (1978); L. F. Wagner, Z. Hussain, and C. S. Fadley, Solid State Commun. 21, 257 (1977).
3. This is the well-known three-step model of photoemission. For a review see D. E. Eastman in Vacuum Ultraviolet Radiation Physics, E. E. Koch, R. Haensel, and C. Kunz, eds. (Pergamon, New York, 1974). Electron transport and transmission through the surface have been neglected.
4. F. R. McFeely, J. Stöhr, G. Apai, P. S. Wehner, and D. A. Shirley, Phys. Rev. B14, 3273 (1976).
5. The crystal potential should remove many of the degeneracies in the high-energy free-electron band structure shown in Fig. 10 of Chapter IV, producing many more bands.
6. a) L. Hodges, H. Ehrenreich, and N. D. Lang, Phys. Rev. 152, 505 (1966);

   b) H. Ehrenreich and L. Hodges in Methods in Computational Physics, B. Alder, S. Fernbach, and M. Rotenberg, eds. (Academic Press, New York, 1968), Vol. 8, p. 149.
7. N. V. Smith, Phys. Rev. B3, 1862 (1971).

8. Neglecting the small spin-orbit coupling for copper, a 9 x 9 matrix was diagonalized at 308 points in the 1/48 irreducible BZ yielding the coefficients $B_{\mu}^{j}(\vec{k})$ where j in a band index and μ characterizes the contributions from the five d-orbital-components.

9. M. Tinkham, Group Theory and Quantum Mechanics (McGraw-Hill, New York, 1964), p. 279.

10. Compare Eqs. (3-35) and (3-36) in Ref. 6b.

11. a) V. V. Nemoshkalenko, V. G. Aleshin, Yu. N. Kucherenko, and L. M. Sheludchenko, Solid State Commun. 15, 1745 (1974); (b) V. V. Nemoshkalenko *et al.*, J. Electr. Spectr. 6, 145 (1975); (c) V. V. Nemoshkalenko *et al.*, Physica Scripta 11, 387 (1975); (d) V. V. Nemoshkalenko *et al.*, Solid State Commun. 16, 755 (1975).

12. Note especially the discrepancy between Eq. (7) here and Eq. (6) in Ref. 11c. This latter equation should properly read

$I_{2g}(\vec{k}) = \left(C_1^n(\vec{k})\right)^2 + \left(C_2^n(\vec{k})\right)^2 + \left(C_3^n(\vec{k})\right)^2$ and

$I_{eg}(\vec{k}) = \left(C_4^n(\vec{k})\right)^2 + \left(C_5^n(\vec{k})\right)^2$. The error made by V. V. Nemoshkalenko *et al.* drastically affects their calculations and tends to make them look close to experiment by suppressing some of the t_{2g} intensity. This is seen in Fig. 4 of Ref. 11c. It is apparent from this figure that a correct calculation including transition martix elements (i.e., adding of e_g and t_{2g} projections in the lower spectrum in Fig. 4) only varies from the density of states insofar as the s-part is suppressed.

13. G. D. Mahan, Phys. Rev. B2, 4334 (1970).

14. S. T. Manson, Phys. Rev. 182, 97 (1969).

15. R. J. Baird, L. F. Wagner, and C. S. Fadley, Phys. Rev. Lett 37, 111 (1976). These authors explained variations observed in ARXPS spectra obtained from Au single crystals in terms of the direct transition model presented in Chapter III of this thesis. More recent calculations, however, by Wehner *et al.* (P. S. Wehner, J. Stöhr, G. Apai, F. R. McFeely, and D. A. Shirley, Phys. Rev. Lett. 38, 169 (1977)) have shown that the matrix-element model presented in this chapter fit their experimentally observed spectra better.

16. R. H. Williams, P. C. Kemeny, and L. Ley, Solid State Commun. 19, 495 (1976).

Table I. Angular d-Orbitals

	Label	Function	
d_1	d_{xy}	$(15/4\pi)^{1/2}\sin^2\theta\sin\phi\cos\phi$	t_{2g}
d_2	d_{yz}	$(15/4\pi)^{1/2}\sin\theta\cos\theta\sin\phi$	
d_3	d_{xz}	$(15/4\pi)^{1/2}\sin\theta\cos\theta\cos\phi$	
d_4	$d_{x^2-y^2}$	$\frac{1}{4}(15/4\pi)^{1/2}\sin^2\theta\cos2\phi$	e_g
d_5	$d_{3z^2-r^2}$	$\frac{1}{2\sqrt{3}}(15/4\pi)^{1/2}(3\cos^2\theta - 1)$	

FIGURE CAPTIONS

Fig. 1 Experimental geometry for angle resolved photoemission studies at 1486.6 eV. The angle between the x-ray incidence- and electron exit-directions was fixed at 72°. Spectra were measured along the [111] direction of a crystal with a (001) surface orientation and along the [001] direction of a crystal with a (001) face.

Fig. 2 (a) Experimental photoemission spectra from valence bands of Cu using AlKα radiation. The first spectrum was obtained with a polycrystalline (evaporated) Cu sample. The second spectrum was measured along the [111] direction, and the third spectrum along the [001] direction of a single crystal.
(b) Comparison of the Cu[111] and Cu[001] spectra of Fig. 1a.
(c) Calculated t_{2g} and e_g projections of the total Cu 3d density of states using a tight binding interpolation scheme as discussed in the text. The density of states histograms were convoluted with a Gaussian of FWHM = 0.8 eV.

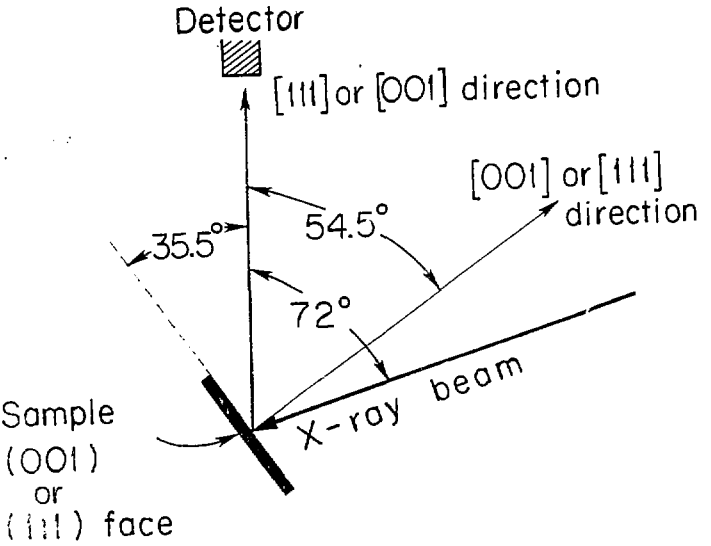

XBL768-3275

Figure 1

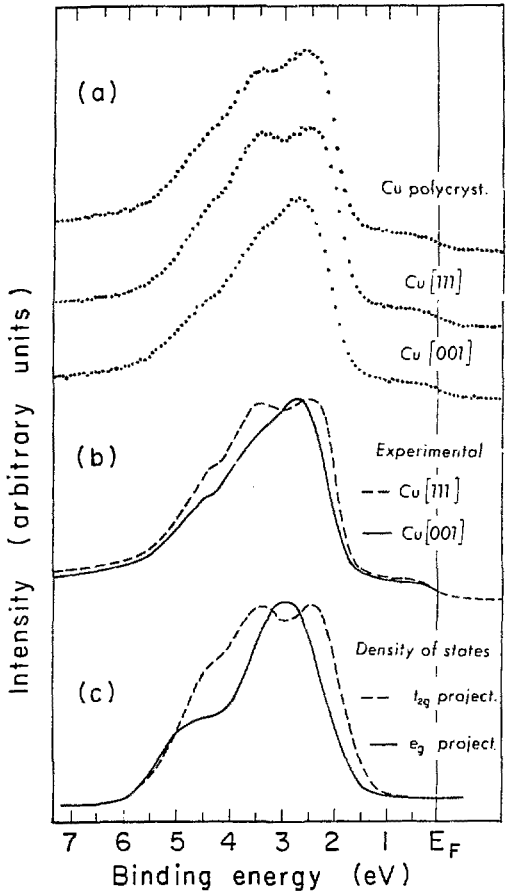

Figure 2

XBL 765 2894

ACKNOWLEDGEMENTS

Many things have contributed to the achievement of my degree, not the least of which has been the support and encouragement given to me by my colleagues and friends, for which I am extremely grateful. It is with particular pleasure that I thank Professor David A. Shirley, who directed the research reported in this thesis, and whose physical insight and extensive knowledge have contributed immensely to my understanding of many aspects of this work.

In addition, I have benefited greatly from numerous discussions with my colleagues in the electron spectroscopy group, to whom I offer my thanks. I am particular indebted to Dr. Joachim Stöhr, Dr. Gus Apai, Dr. Read McFeely, and Dr. R. Stanley Williams. I have also had the pleasure of working with and learning from Dr. Richard Martin, Dr. Shuit-Tong Lee, Dr. O. B. Dabbousi, Steve Kevan, Rich Davis, Dave Denley, Richard Rosenberg, Erwin Poliakoff, Mike White, Dennis Trevor, and Ken Mills.

The support staff at LBL have been very generous with their talents and advice. Gene Miner, Joseph Katz, Richard Strudwick, and D. N. Voronin have provided valuable technical assistance throughout my graduate career, for which I am in their debt. I am also sincerely grateful to Karen Janes and Wini Heppler for their many contributions in typing manuscripts, preparing samples, and in making LBL a very pleasant place to work.

I would also like to thank Carol Smith for her numerous suggestions concerning the cleaning and preparation of Pt single crystals, and Ken Mills for his careful reading of this manuscript and his many editorial

comments.

Since life consists of more than science, I must acknowledge those people who have given it special meaning to me. To the Leventhals - Alexandra, Leon, Margret, Daniel, Jeanne, and Harald - my profound gratitude for the friendship they have given me during the past four years, and for opening their home to me. To Mary Jo and Richard Waters, who have been very close friends for many years, my special thanks. And to my parents, my undying gratitude and love for their constant support and encouragement.

Work supported by the U. S. Department of Energy.